IVYSPRING INTERNATIONAL PUBLISHER

International Journal of Biological Sciences

2027; 23(1): 640-662. doi: 10.7150/ijbs.143309

Research Paper

TRIM25-mediated ubiquitination and degradation of NSUN2 promotes ferroptosis in nucleus pulposus cells by decreasing m5C methylation of *Fth1* mRNA

Peng Cui[1,2,3*], Tao Hu[1,2*], Qingyang Huang[1,2*], Yijian Zhang[4*], Xuan Zhao[1,2], Haojie Zhang[1,2], Fumin Pan[1,2], Chao Kong[1,2], Ruizhang Yao[1,2], Yuluo Rong[3], Jiaxiang Bai[3], Haixia Huang[5], Peng Wang[1,2✉], Yongjin Li[3✉], Xiaolong Chen[1,2✉], Shibao Lu[1,2✉]

1. Department of Orthopaedics, Xuanwu Hospital, Capital Medical University, Beijing, China.
2. Laboratory for Clinical Medicine, Capital Medical University, Beijing, China.
3. Department of Orthopaedics, The First Affiliated Hospital of USTC, Division of Life Sciences and Medicine, University of Science and Technology of China, Hefei, Anhui, China.
4. Senior Department of Hematology, the Fifth Medical Center of PLA General Hospital, Beijing 100071; Beijing Key Laboratory of Hematopoietic Stem Cell Therapy and Transformation Research, Beijing 100071, China.
5. Department of Physiology and Pathophysiology, School of Basic Medical Sciences, Capital Medical University, Beijing, China.

* These authors contributed equally.

✉ Corresponding authors: Peng Wang (wpspine@sina.com), Yongjin Li (Yongjin816@ustc.edu.cn), Xiaolong Chen (chensmalldragon@163.com) and Shibao Lu (LSBspine@163.com).

© 2027 The Author(s). This is an open access article distributed under the Creative Commons Attribution 4.0 International Licence, subject to the Publisher's Terms of Use at https://ivyspring.com/terms.

Received: 2026.08.29; Accepted: 2026.10.28; Published: 2027.01.01

Abstract

Intervertebral disc degeneration (IVDD) represents a major cause of chronic low back pain, yet the regulatory circuits involved in nucleus pulposus cells (NPCs) homeostasis remain inadequately characterized. This study identifies a previously uncharacterized TRIM25-NSUN2-FTH1 axis that drives ferroptosis in NPCs, thereby orchestrating IVDD progression. NSUN2, a key 5-methylcytosine (m5C) methyltransferase, is markedly downregulated in degenerated human NP tissues. Mechanistically, NSUN2 deposits m5C onto ferritin heavy chain 1 (*Fth1*) mRNA, which is recognized by the reader protein Ybox binding protein 1 (YBX1), thereby stabilizing the transcript and maintaining FTH1 expression. Immunoprecipitation-mass spectrometry (IP/MS) analysis indicated that the E3 ubiquitin ligase TRIM25 directly interacts with NSUN2, facilitating its Lys48-linked polyubiquitination and subsequent proteasomal degradation. This degradation diminishes m5C modification of *Fth1* mRNA, resulting in FTH1 depletion, labile iron overload, lipid peroxidation, and mitochondrial dysfunction, rendering NPCs more susceptible to ferroptosis. Notably, genetic silencing of TRIM25 or overexpression of NSUN2 effectively restores FTH1 levels, suppresses ferroptosis and attenuates disc degeneration in a rat IVDD model. Overall, these findings elucidate a critical interplay between ubiquitin-mediated protein turnover and epitranscriptomic regulation in ferroptosis control, establishing TRIM25 as a potential therapeutic target for IVDD.

Keywords: 5-methylcytosine methyltransferase, ubiquitination; ferroptosis; intervertebral disc degeneration; nucleus pulposus cell; NSUN2; TRIM25

Introduction

Intervertebral disc degeneration (IVDD) represents a leading cause of low back pain, constituting a significant public health concern that imposes considerable socioeconomic burden globally[1]. Characterized by the progressive breakdown of the extracellular matrix (ECM) in the nucleus pulposus (NP), IVDD is driven by a complex interplay of biochemical and biomechanical factors, including aberrant inflammation, excessive oxidative stress, and the progressive loss of NP cells (NPCs)[2-7]. Despite its high prevalence, existing therapeutic strategies for IVDD primarily focus on symptomatic

relief and fail to address the underlying pathophysiological processes[8-10]. Therefore, a deeper understanding of the molecular mechanisms governing NPCs homeostasis and degeneration is urgently needed to identify novel therapeutic targets.

Ferroptosis, a recently identified form of regulated cell death driven by iron-dependent lipid peroxidation, has emerged as a critical contributor to the pathogenesis of various degenerative and inflammatory diseases[2, 4, 5, 11-13]. Unlike apoptosis or necrosis, ferroptosis is characterized by distinct morphological and biochemical features, including mitochondrial shrinkage, increased mitochondrial membrane density, and the accumulation of lethal lipid reactive oxygen species (ROS)[14, 15]. Emerging evidence has implicated ferroptosis in the progression of musculoskeletal disorders, including osteoarthritis and osteoporosis[16-21]. In IVDD, recent studies have begun to reveal that ferroptosis is activated in degenerated NP tissues and contributes to NPCs loss and extracellular matrix degradation[11]. Multiple pathological stimuli in the degenerative disc microenvironment, such as mechanical overload, oxidative stress, inflammation, and iron overload, can trigger ferroptosis in NPCs[4, 5, 14, 22]. Mechanistically, dysregulation of key ferroptosis regulators, including GPX4, ACSL4, SLC7A11, and NCOA4-mediated ferritinophagy, has been associated with IVDD progression[2, 16, 23]. Although these studies have established a role for ferroptosis in IVDD, the upstream regulatory circuits that initiate and amplify ferroptosis in NPCs, particularly those linking post-translational modifications and epitranscriptomic regulation, remain incompletely understood. Considering that NPCs are vital for maintaining the homeostasis of the avascular intervertebral disc (IVD), preventing their ferroptosis may represent a promising therapeutic avenue[19].

RNA modifications have emerged as critical regulators of diverse biological processes and are increasingly recognized for their involvement in the pathogenesis of various diseases, including degenerative disorders[24-29]. Among the more than 170 known types of RNA modifications, 5-methylcytosine (m5C) constitutes a prevalent epitranscriptomic mark that regulates RNA stability, translation, and splicing[30, 31]. NSUN2, a key member of the NOL1/NOP2/Sun domain family, functions as a major methyltransferase catalyzing m5C modification on messenger RNAs (mRNAs). Recent studies have demonstrated that NSUN2-mediated m5C methylation plays pivotal roles in cell proliferation, differentiation, and stress responses[32-37]. NSUN2-mediated m5C methylation has been reported to regulate diverse biological processes in multiple cell types. In embryonic development, NSUN2 is required for self-renewal and differentiation, as disruption of m5C regulatory often causes developmental defects, underscoring its critical role during embryogenesis[33]. In hepatocytes, degradation of NSUN2 decreases the stability of GPX4 mRNA, thereby inducing ferroptosis[38]. In gastric cancer cells, upregulation of NSUN2 promotes the proliferation, migration, and invasion of GC cells[35]. In kidney cells, downregulation of NSUN2 promotes mitochondrial fission and thereby accelerates renal fibrosis[37]. These findings indicate that NSUN2 functions in a cell-type- and context-dependent manner. However, the function of NSUN2 and m5C modification in the context of IVDD and ferroptosis regulation have yet to be investigated.

Post-translational modifications (PTMs) constitute a key mechanism of cellular regulation, governing protein fate through dynamic and reversible molecular processes[2, 12, 22, 24, 39, 40]. Among these, ubiquitination and deubiquitination constitute a finely tuned regulatory circuit that regulates protein turnover, intracellular trafficking, and functional activation, thereby exerting profound influences on cell survival and autophagic processes[16, 38, 41, 42]. Briefly, E3 ubiquitin ligases, which confer substrate specificity, directing proteins toward proteasome-dependent degradation, and deubiquitinating enzymes (DUBs), which counteract this signal by stripping ubiquitin chains from modified proteins. PTMs are intricately linked to the pathophysiology of IVDD[23, 40-42]. Our previous study has demonstrated that UCHL3, acting as a DUB, stabilizes HMGB1, which subsequently activates NCOA4-mediated ferritinophagy, exacerbating IVDD[23]. TRIM25 is a member of the tripartite motif (TRIM) family of E3 ubiquitin ligases. It has been implicated in the regulation of innate immunity, antiviral responses, and tumorigenesis through its ubiquitin ligase activity[43-46]. Nevertheless, the role of TRIM25 in degenerative musculoskeletal disorders, particularly concerning the regulation of ferroptosis and NPCs homeostasis, remains uninvestigated.

This study identifies a previously uncharacterized TRIM25-NSUN2-FTH1 signaling axis that drives ferroptosis in NPCs and accelerates IVDD progression. Notable findings reveal that NSUN2 is markedly downregulated in degenerated human NP tissues and that its loss promotes ferroptosis through diminished m5C methylation of *Fth1* mRNA, leading to reduced FTH1 protein expression and subsequent susceptibility to ferroptosis. Mechanistically, we show that the E3 ubiquitin ligase TRIM25 directly interacts with NSUN2 and mediates its Lys48-linked polyubiquitination and proteasomal degradation,

thereby suppressing NSUN2 protein levels during ferroptosis and IVDD. The m5C reader YBX1 recognizes the methylated *Fth1* transcript and preserves its stability, and this protective axis is compromised following NSUN2 degradation. Importantly, genetic silencing of TRIM25 *in vivo* restores NSUN2 expression, enhances m5C methylation of *Fth1* mRNA, elevates FTH1 protein abundance, and attenuates IVDD progression in a rat model. Collectively, these findings delineate a novel molecular pathway coupling ubiquitin-mediated degradation of an m5C methyltransferase to ferroptosis susceptibility in NPCs, position TRIM25 as a potential therapeutic target for IVDD, and provide a mechanistic foundation for developing disease-modifying therapies for disc degeneration and associated low back pain.

Methods and Materials

The acquisition of human NP tissue

Human NP tissues were obtained from patients at Xuanwu Hospital, Capital Medical University, following informed consent (Approval No. XW-2024-010-001). Based on preoperative MRI, these tissues were categorized into Pfirrmann grades I, III, and V.

Cell culture and transfection

NPCs were isolated from intervertebral disc (IVD) tissue samples of patients with Pfirrmann grades I-II using type II collagenase digestion. The NPCs were cultured in DMEM/F12 medium (Gibco, Thermo Fisher Scientific 11,330,057) supplemented with 10% fetal bovine serum (FBS, Gibco 10,099-141C) and 1% penicillin-streptomycin (Beyotime, C0222), and maintained in T25 flasks at 37 °C in a humidified atmosphere containing 5% CO_2. HEK 293T cells (Pricella Life Science & Technology Co., Ltd, CL-0005) were cultured under the same conditions in DMEM with 10% FBS and 1% penicillin-streptomycin. To evaluate NSUN2 protein stability, NPCs were treated with 10 μM cycloheximide (CHX; MedChemExpress, HY-12320) at 0, 2, 4 and 8 hours according to our preliminary time-course experiments, with or without 10 μM erastin (MedChemExpress, HY-15763) stimulation, to block protein synthesis; additionally, NPCs were treated with 20 μM MG132 (MedChemExpress, HY-13259) to inhibit proteasomal degradation. Transfections were performed using Lipofectamine 2000 (Invitrogen) according to the manufacturer's instructions. The knockdown or overexpression efficiency was verified by Western blot and qPCR. The targeted sequences of shRNA or si-RNA used in this study were as follows: shNSUN2: 5′-GCTGGCACAGGAGGGAATATA-3′; shTRIM25: 5′-GCTTTCGAGACGATGATTATT-3′; si-YBX1: 5′-GGCAATGAAGAAGATAAAGAAAA-3′.

Total RNA isolation and RT-qPCR

Total RNA extraction was performed using TRIzol Reagent (Life Technologies, Carlsbad, CA, USA), and 1 μg was reverse-transcribed using a cDNA synthesis kit (Thermo Fisher Scientific, Massachusetts, USA). The resulting cDNA was then subjected to RT-qPCR, with *β-actin* serving as the internal reference for normalizing target gene mRNA expression. Relative transcript abundance was determined by the $2^{-\Delta\Delta Ct}$ method. Primer sequences for RT-qPCR are provided in the Supplementary Table 1.

RNA dot blot assay

RNA samples were heated at 75 °C for 5 minutes and immediately placed on ice. Indicated amounts of RNA were spotted onto nylon membranes (Solarbio, YA1760), which were then crosslinked under UV light for 5 minutes, blocked with 5% non-fat milk for 2 hours, and washed three times with TBST. The membranes were incubated overnight at 4 °C with anti-m5C antibody, followed by incubation with a secondary antibody for 1.5 hours and two TBST washes. Signals were developed using ECL substrate. After development, the membranes were washed twice with TBST and stained with 0.02% methylene blue (Shanghai yuanye Bio-Technology Co., Ltd, R27236).

RNA stability

RNA stability was evaluated using actinomycin D (Act-D). Briefly, cells were treated with Act-D at a final concentration of 5 μg/mL (added as 2.5 μL of a 2 mg/mL stock solution per 1 mL of medium) after transfection, then harvested at 0, 2, 4, 6 and 8 hours for total RNA extraction. The mRNA levels of *Fth1* were quantified by RT-qPCR.

RNA immunoprecipitation (RIP) and MeRIP-seq

RIP was performed using the Magna RIP RNA-Binding Protein Immunoprecipitation Kit (Millipore, Bedford, MA, USA) according to the manufacturer's instructions with IgG was used as a negative control. Cell lysates were incubated with 5 μg of anti-m5C antibody or IgG as a control. Briefly, the antibody was mixed with 50 μL of Protein G magnetic beads (Thermo Fisher Scientific) and rotated for 15 minutes, followed by overnight incubation with the lysates at 4 °C on a rotator. The immunoprecipitated RNA was then released by Proteinase K (Beyotime, ST535) digestion, purified with RNA purification beads (Beyotime, R0081), and subsequently subjected to

reverse transcription and quantitative PCR.

In vitro methylation site assays

Bisulfite exposure deaminates cytosine lacking methylation, transforming it to uracil (U), whereas cytosine carrying a methyl group remains unaltered. To investigate the precise methylation site, total RNA was extracted from NPCs using TRIzol, fragmented, followed by fragmentation and converted via bisulfite treatment with the EZ RNA Methylation Kit (Zymo Research). The converted RNA was used to construct strand-specific libraries with the KC-DigitalTM kit (SeqHealth, Wuhan, China) and subjected to high-throughput sequencing. Raw FASTQ reads were quality-filtered, and the clean reads were aligned to the reference genome using Bismark v0.23.1, which performed alignment, deduplication and methylation calling; the methylation level was determined using the formula mC/(mC+μmC) according to previously reported[37]. Metilene (v0.2-8) was applied to identify differentially methylated regions (DMRs) for paired samples or between two groups. DMRs across groups were called using Metilene (v0.2-8).

Western blot analysis

NP tissues and NPCs were homogenized and lysed in RIPA lysis (Beyotime, P0013B) buffer supplemented with 1% protease and phosphatase inhibitor cocktail (Beyotime, P1049). After centrifugation at 14,000×g for 30 minutes, the supernatant was collected, and protein concentrations were determined using a BCA protein assay kit (Beyotime, P0012S). Proteins were separated by SDS-PAGE and transferred onto PVDF membranes. The membranes were blocked with 5% non-fat milk for 2 hours at room temperature, followed by incubating overnight at 4 °C with primary antibodies, and then with the corresponding fluorescently labelled secondary antibodies for 1 hour at room temperature. For chemiluminescence detection, the chemiluminescent substrate was applied directly to the membrane regions corresponding to the target proteins. Band intensities were quantified using ImageJ software based on densitometric values (grey density). Details of the antibodies used are listed in Supplementary Table 2.

Immunofluorescence

NPCs cultured *in vitro* were seeded in 24-well plates. Following cell attachment and the designated interventions, the medium was removed, and the cells were rinsed twice with PBS, fixed with 4% paraformaldehyde for 15 minutes at room temperature, and permeabilized with 0.1% Triton X-100 (Beyotime, P0096) for 5 minutes at room temperature. Non-specific binding sites were blocked with 10% goat serum (Solarbio, SL038) for 1 hour. The blocking solution was aspirated, and the cells were incubated with appropriately diluted primary antibodies overnight at 4 °C. After thorough washing with PBS, the cells were incubated with the corresponding fluorescently labelled secondary antibodies for 1 hour at 37 °C in the dark. Nuclei were counterstained with DAPI (Beyotime, C1006) for 5 minutes at room temperature in the dark. Fluorescence images were acquired using a fluorescence microscope, and the fluorescence intensity of the target protein was quantified with ImageJ software.

Cell viability analysis

For cell viability assays, NPCs were seeded into 96-well plates at a density of 1×10^4 cells per well. After cell attachment and completion of the designated interventions, the supernatant was discarded and replaced with fresh medium. CCK-8 reagent (Beyotime, C0038) was then added to each well following the manufacturer's instructions. The plates were incubated at 37 °C for 3 hours, and the absorbance at 450 nm was measured using a microplate reader to assess cell viability across the different treatment groups.

Calcein-AM/PI staining

NPCs were seeded into 24-well plates at an appropriate density. After the designated treatments, 250 μL of Calcein-AM/PI working solution (Beyotime, C2015M) was added to each well, and the plates were incubated at 37 °C in the dark for 30 minutes. Live and dead cells were then visualized under a fluorescence microscope, and fluorescence intensities were quantified using ImageJ software.

Enzyme-linked immunosorbent (ELISA) assay

Following the indicated treatments, cell lysates or tissue homogenates from experimental groups were prepared according to the manufacturer's protocols, and the levels of malondialdehyde (MDA), glutathione (GSH), and Fe^{2+} in the homogenates were quantified using commercial kits (MDA: Westang, F01963; GSH: Westang, G02170; Fe^{2+}: Westang, G01670).

FerroOrange Fe^{2+} staining

Intracellular labile Fe^{2+} levels were measured using the FerroOrange probe (Dojindo, F374), as previously described[23]. Briefly, NPCs were incubated with 10 μM FerroOrange for 30 minutes at 37 °C in a 5% CO_2 incubator, followed by fluorescence imaging and fluorescence signals were subsequently quantified

with ImageJ software.

JC-1 measurement

Mitochondrial membrane potential was assessed using the JC-1 probe (Beyotime, C2006). Briefly, at high membrane potential, JC-1 forms J-aggregates in the mitochondrial matrix that emit red fluorescence; whereas at low membrane potential, JC-1 exists as monomers that emit green fluorescence. The red-to-green fluorescence ratio provided a measure of mitochondrial depolarization.

ROS detection

Intracellular ROS levels were assessed using the DCFH-DA probe (Beyotime, S0033M). Briefly, after NPCs were exposed to the indicated treatments, cells were incubated with DCFH-DA at 37 °C in the dark for 20 minutes, washed thoroughly to remove unbound probe, and then analysed by flow cytometry for fluorescence intensity using FlowJo software.

Mitochondrial superoxide assay

Mitochondrial superoxide production was measured using the MitoSOX Red probe (Beyotime, S0061S). After removing the culture medium and washing the cells with PBS, NPCs were incubated with 5 μM MitoSOX Red at 37 °C in the dark for 30 minutes. Following two washes with PBS, fluorescence signals were examined under a fluorescence microscope, with red fluorescence intensity serving as an indicator of mitochondrial superoxide levels.

Lipid peroxidation assay

Lipid peroxidation was quantified using the fluorescent probe BODIPY 581/591 C11 (Invitrogen, D3861). After aspirating the culture medium, NPCs were incubated with 2 μM BODIPY 581/591 C11 at 37 °C for 20 minutes. The supernatant was then removed, and the cells were washed twice with PBS. Fluorescence signals were visualized under a fluorescence microscope, with the probe emitting red fluorescence in its reduced state and green fluorescence upon oxidation. The red-to-green fluorescence ratio thus indicated the degree of lipid peroxidation.

Mitochondria staining

Mitochondrial morphology in NPCs was evaluated using Mito-Tracker Green (Beyotime, C1048). The working solution was prepared as per the manufacturer's instructions and pre-warmed to 37 °C. After the culture medium was removed, NPCs were incubated with the pre-warmed Mito-Tracker Green working solution at 37 °C for 30 minutes. The staining solution was replaced with fresh culture medium pre-warmed to 37 °C, and mitochondrial morphology and distribution were observed under a confocal microscope.

TEM for mitochondrial morphology in NPCs

Cell pellets were fixed with 2.5% glutaraldehyde, dehydrated through graded ethanol and acetone, and embedded in epoxy resin. The resin blocks were polymerized at 65 °C for over 48 hours and then stored at room temperature. Ultrathin sections (75 nm) were cut using an ultramicrotome, stained with 2% uranyl acetate in ethanol (8 minutes in the dark) and 2.6% lead citrate (8 minutes in the dark), and examined under a Hitachi HT7800 electron microscope.

Co-immunoprecipitation (Co-IP)

NPCs were lysed in IP-specific lysis buffer supplemented with protease and phosphatase inhibitors, along with PMSF. Following centrifugation at 15,000 rpm for 10 minutes at 4 °C, the supernatants were incubated with protein A/G-conjugated magnetic beads and antibodies targeting the protein of interest. Immune complexes were eluted, then separated via SDS-PAGE and transferred onto PVDF membranes. Western blot analysis was conducted as previously described, with band intensities quantified using ImageJ software.

Immunoprecipitation-mass spectrometry (IP/MS)

The protein fractions eluted from immunoprecipitation were separated by SDS-PAGE, and the target protein bands (approximately 1 mm^3) were excised. The gel pieces were destained, reduced with dithiothreitol, and alkylated with iodoacetamide to block free cysteine thiols, followed by overnight in-gel digestion with trypsin. The resulting peptide mixtures were fractionated by gradient elution using nano-flow capillary high-performance liquid chromatography and then analyzed on a Thermo Scientific Q Exactive HF-X high-resolution tandem mass spectrometer operated in data-dependent acquisition mode. The raw MS data were processed with Proteome Discoverer 3.0 software against the reference protein sequence database of the corresponding species, enabling confident identification of peptide sequences and their originating proteins.

Construction of IVDD model

Adult rats (weighing 250 ± 20 g) were purchased from Beijing Vital River Laboratory Animal Technology Co., Ltd. and housed in the Animal Experimental Center of Xuanwu Hospital, Capital Medical University. A rat model of IVDD was

established by annular needle puncture following a previously reported protocol[23]. Briefly, rats were anesthetized with isoflurane, and the seventh and eighth coccygeal vertebrae (Co7/8) were identified by X-ray guidance. A 22-gauge needle was then inserted through the annulus fibrosus into the nucleus pulposus to a depth of 5 mm, with the needle trajectory maintained perpendicular to the disc plane. To induce standardized disc injury, the needle was rotated 360° and kept in place for 30 seconds. Sham animals underwent the same surgical exposure and Xray guidance without needle puncture. All animal procedures were approved by the Institutional Animal Care and Use Committee of Xuanwu Hospital of Capital Medical University (Approval No. XW-20251022-1).

Adeno-associated virus (AAV) infection

Six- to eight-week-old rats were randomly assigned to experimental groups using a computer-generated randomization method. Following anaesthesia with isoflurane, 1 μL of the respective tool viruses (AAV-vec, AAV-NSUN2, AAV-shCtrl or AAV-shTRIM25), each at a packaged titer of 1.5×10^{12} v.g./mL, was precisely injected into the NP of the tail intervertebral discs at the Co7/8 level using a 33-gauge Hamilton microsyringe. Injections were performed once weekly for four consecutive weeks to achieve targeted delivery. Two months after the final injection, the animals were euthanized, and disc tissues from the targeted segments were collected for subsequent imaging and histological analyses. All AAV vectors used in this study were provided by GenePharma (Shanghai, China).

X-ray and MRI

To radiologically examine intervertebral discs, rats were anesthetized with sodium pentobarbital (40 mg/kg, 10% solution) intraperitoneally and placed prone for both radiography and MRI. X-ray images were captured at 160 mA and 50 kV, while T2-weighted MR scans were performed on a 3.0-T Siemens clinical system to evaluate disc morphology, and hydration. The degree of IVDD was quantified using Pfirrmann grading and disc height index (DHI) scores derived from the acquired images.

Hematoxylin and eosin (H&E), safranin o & fast green (SO-FG) and Alcian blue staining

Collected IVD specimens were fixed in 4% paraformaldehyde for 72 hours, fully decalcified in 10% EDTA (pH 7.4) at 37 °C for 4 weeks, then embedded in paraffin and sectioned into 5 μm-thick coronal slices. Routine H&E staining was performed to distinguish intact disc architecture, with semiquantitative degeneration grading conducted following the Pfirrmann criteria. Safranin O-Fast Green staining specifically labels proteoglycans and collagen fibers, and ImageJ software was applied to quantify the positive IOD ratio in the nucleus pulposus. Alcian Blue staining visualizes the distribution of extracellular acidic glycosaminoglycans. All sections were digitally scanned, and examined under a light microscope for structural and compositional analysis.

Immunohistochemistry (IHC) staining

Following deparaffinization and rehydration, 5 μm-thick disc tissue sections underwent high-temperature antigen retrieval in 10 mM citrate buffer for 15 minutes, followed by incubation in 3% hydrogen peroxide for 10 minutes to inhibit endogenous peroxidase activity. Blocking of nonspecific binding was achieved with 5% normal goat serum at room temperature for 1 hour. Sections were then incubated overnight at 4 °C with primary antibodies targeting proteins (NSUN2, ACSL4, GPX4, MMP3, Collagen II, FTH1, and YBX1), followed by a horseradish peroxidase-conjugated secondary antibody for 1 hour at 37 °C. After DAB color development and hematoxylin counterstaining, sections were dehydrated and mounted. Immunoreactivity was visualized using a standard detection system and assessed under light microscopy.

Statistical analysis

All data are presented as mean ± standard deviation (mean ± SD). Comparisons between groups were performed using two-tailed Student's t-test or ANOVA, as appropriate. When one-way ANOVA indicated significant differences among groups, Tukey's post hoc test was used for pairwise comparisons. Graphical and statistical analyses were carried out with GraphPad Prism version 9. Significance levels are denoted as $^{*}p < 0.05$, $^{**}p < 0.01$, and $^{***}p < 0.001$; "ns" indicates no statistical significance.

Results

NSUN2 expression is downregulated in human NPCs after IVDD

To investigate the potential role of m5C modification in IVDD, we performed a preliminary analysis of key m5C regulatory genes based on single-cell database (GSE251686)[47]. We found that NSUN2, a key protein catalyzing mRNA m5C methylation, was significantly decreased during IVDD. Briefly, IVD tissues were stratified into mild and severe degeneration based on T2-weighted MRI using

Pfirrmann grades. Unbiased clustering of all cells was performed by principal component analysis (PCA) and visualised using Uniform Manifold Approximation and Projection (UMAP). Six distinct cell clusters representing different cell types were identified (Figure S1A). NSUN2 was predominantly expressed in NPCs (Figure S1B), and its expression level was significantly reduced in the severe degeneration group (Figure S1C, D). Consistent results emerged from analyses of two independent transcriptomic datasets (GSE245147[3] and GSE266883[48]), which confirmed downregulation of NSUN2 in IVDD samples (Figure S1E, F). Moreover, KEGG and GO enrichment analyses of the top 30 genes most highly correlated with NSUN2 suggested its potential involvement in ferroptosis within NPCs (Figure S1G, H).

Reduced NSUN2 expression is accompanied by ferroptosis after IVDD

To investigate changes in NSUN2 expression, we collected NP tissues from patients with IVDD, stratified according to the Pfirrmann grading system, for H&E staining (Figure 1A). Concurrently, global m5C levels in total RNA extracted from these tissues were quantitatively assessed using the EpiQuik m5C RNA Methylation Quantification Kit and validated by dot blot analysis. Notably, RNA m5C levels exhibited a marked decline in parallel with advancing IVDD (Figure 1B, C). IHC assessment of NSUN2, IVDD-related markers (Collagen II and MMP3) and ferroptosis-related markers (FTH1 and ACSL4) showed that NSUN2 expression correlated inversely with Pfirrmann grade, MMP3 and ACSL4, while correlating positively with Collagen II and GPX4 (Figure 1D, E). Western blot analysis of tissue lysates from IVDD demonstrated a progressive loss of NSUN2, anabolic ECM components (Aggrecan and Collagen II), and the ferroptosis-related indicators (FTH1 and GPX4), paralleled by an increase in catabolic mediators (MMP3 and MMP13), ACSL4 and PTGS2 as disease severity escalated (Figure 1F-J). Immunofluorescence of NSUN2 further corroborated these findings (Figure 1K, L). Collectively, these findings indicated that NSUN2 expression is associated with enhanced ferroptosis-related changes and increased severity of IVDD.

Overexpression of NSUN2 decreases NPCs ferroptosis *in vitro*

To evaluate the involvement of NSUN2 in NPCs ferroptosis, a panel of ferroptosis markers were measured in NSUN2-silenced or NSUN2-overexpressed cells under erastin-induced conditions. Western blot confirmed that sh-NSUN2 significantly decreased, whereas OE-NSUN2 significantly increased, the level of NSUN2 protein (Figure 2A, B and Figure S2A, B). Dot blot assays revealed that knockdown of NSUN2 led to a decrease in m5C methylation levels, while overexpressing NSUN2 resulted in an increase in m5C methylation levels (Figure 2C). Further analysis indicated that NSUN2 knockdown markedly elevated the levels of MDA, lipid peroxidation, intracellular ROS, and Fe^{2+}, accompanied by a decline in GSH (Figure 2D-I and Figure S2F, G). In contrast, overexpression of wild-type NSUN2 effectively mitigated these changes and replenished GSH, however, overexpression of the methyltransferase-dead mutant NSUN2 C321A failed to recapitulate these protective effects (Figure 2D-I and Figure S2F, G). Additionally, NSUN2 knockdown reduced cell viability, overexpression of wild-type NSUN2 partially rescued the suppression of cell viability, whereas catalytically dead NSUN2 mutant (C321A) failed to exert any appreciable effect (Figure S2C-E). Western blot analysis further substantiated that overexpression of wild-type NSUN2 mitigates NPCs ferroptosis, as evidenced by decreased ACSL4 and PTGS2 expression levels and increased FTH1 and GPX4 expression, effects that were completely abrogated by the C321A mutant (Figure 2J, K). Western blot for IVDD-related markers further substantiated these observations (Figure S4I, J). Given the established relationship between ferroptosis and mitochondrial function, we next detected mitochondrial morphology and functional changes upon NSUN2 knockdown or overexpression. MitoSOX Red fluorescence assays revealed that NSUN2 knockdown markedly elevated mitochondrial superoxide accumulation, whereas wild-type NSUN2 overexpression reduced it (Figure 2L, M). JC-1 analysis further demonstrated that NSUN2 silencing caused pronounced mitochondrial depolarization, which was rescued by overexpression of wild-type NSUN2 (Figure 2N, O). Similar results were further confirmed by Mito Tracker staining (Figure S4H). Furthermore, transmission electron microscopy (TEM) imaging confirmed that knockdown of NSUN2 provoked severe mitochondrial ultrastructural abnormalities, typified by cristae rupture and outer membrane alterations; these defects were largely reversed by overexpression of wild-type NSUN2 (Figure 2P). Notably, the catalytically dead C321A mutant failed to confer these protective effects (Figure 2L-P). In addition, to further clarify the correlation between NSUN2 and ferroptosis, rescue experiments were also conducted. We found that RSL3, another ferroptosis inducer, effectively induced ferroptosis in NPCs, whereas NSUN2 overexpression significantly prevented ferroptosis (Figure S3A-N). Similarly, the

ferroptosis inhibitor Fer-1 effectively alleviated NSUN2 knockdown-induced ferroptosis (Figure S4A-N). Collectively, these observations implicated that the m5C methyltransferase activity of NSUN2 is indispensable for both the maintenance of mitochondrial homeostasis and the protection of NPCs from ferroptosis.

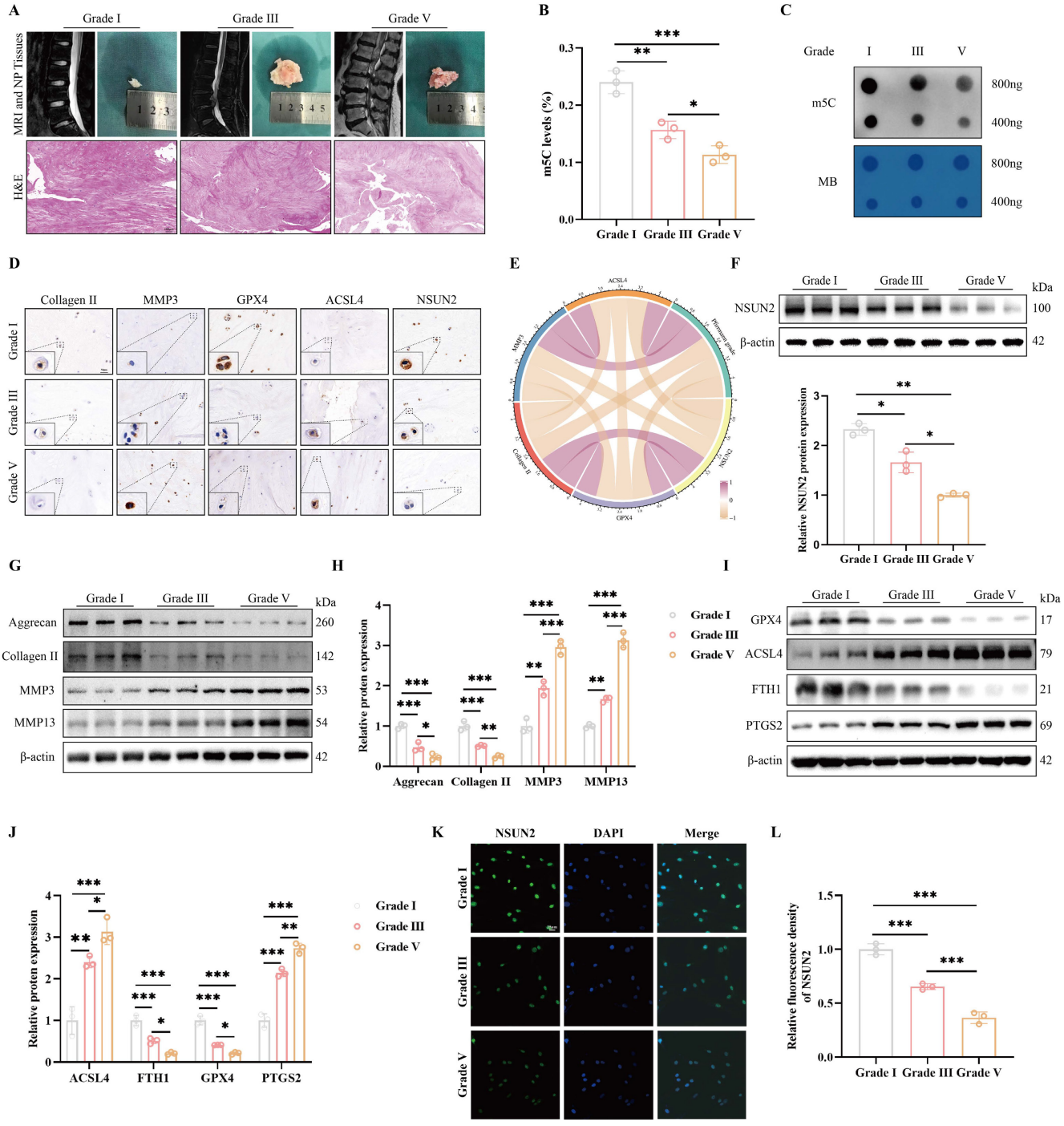

Figure 1. NSUN2 is downregulated, accompanied by the occurrence of ferroptosis in degenerated NP tissues. (A) Representative images and H&E staining of human NP tissues stratified by Pfirrmann grade on T2-weighted MRI (scale bar: 100μm). (B) m5C ELISA was performed to assess m5C RNA methylation levels in human NP tissues (n = 3). (C) Dot blot assay was used to assess m5C RNA modification levels. (D) Representative IHC staining (Collagen II, MMP3, GPX4, ACSL4 and NSUN2) of human NP tissues (scale bar: 50μm; n = 3). (E) Correlation analysis of IHC positivity rates. (F) The protein levels of NSUN2 detected by western blot in human NP tissues (n = 3). (G, H) Western blot of Aggrecan, Collagen II, MMP3 and MMP13 expression in human NP tissues (n = 3). (I, J) Western blot of GPX4, ACSL4, FTH1 and PTGS2 expression in human NP tissues (n = 3). (K, L) The immunofluorescence staining of NSUN2 on human NP tissues (scale bar: 25μm; n = 3). Data are presented as the mean ± SD. *p < 0.05, **p < 0.01, ***p < 0.001.

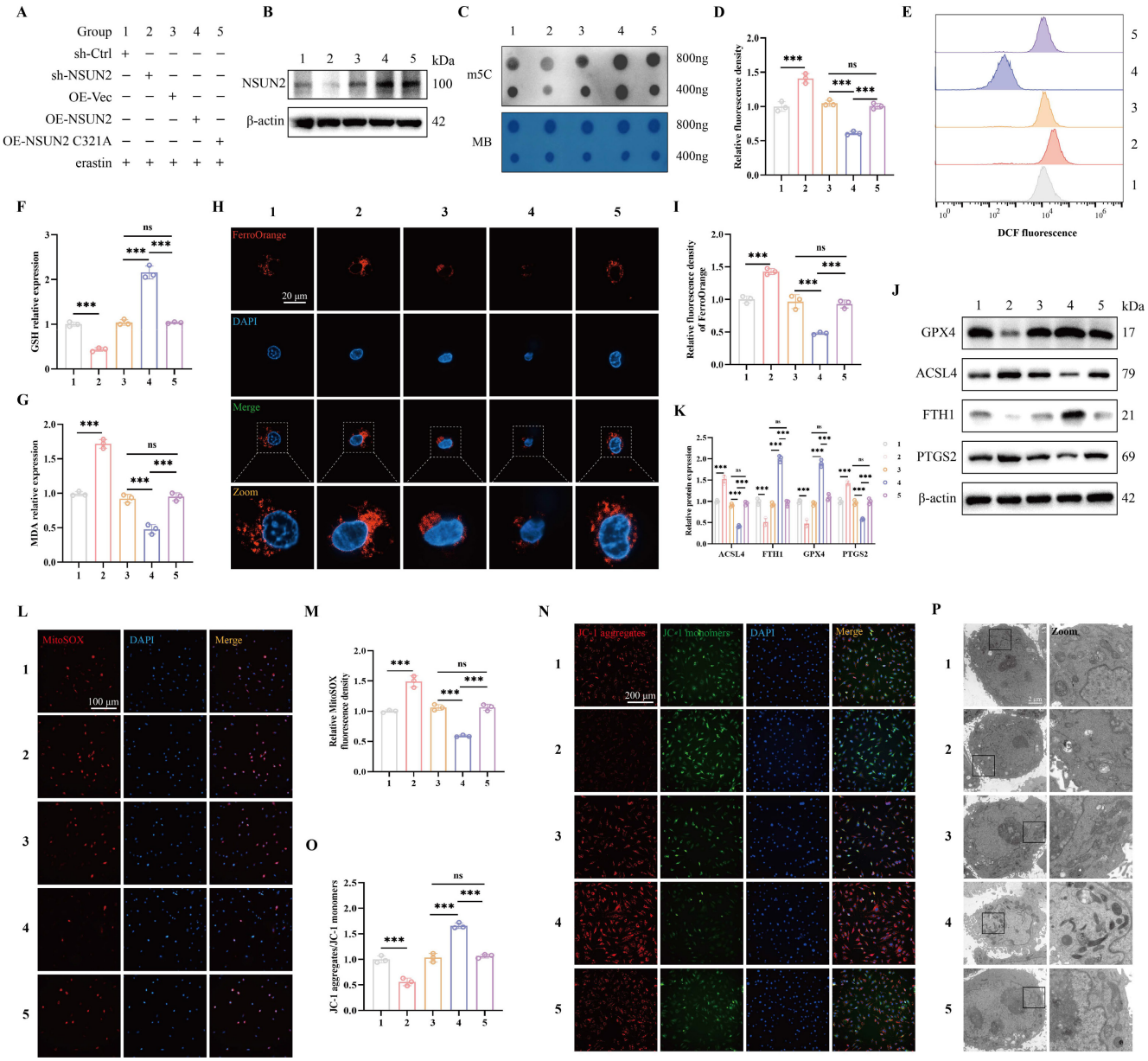

Figure 2. Knockdown of NSUN2 promotes NPCs ferroptosis *in vitro*. (A) Experimental assignment. (B) The transfection efficiency was confirmed by western blot analysis (n = 3). (C) Dot blot assay was used to assess m5C levels in NSUN2 knockdown or NSUN2 overexpression NPCs. (D-G) ROS, GSH and MDA concentrations were measured (n = 3). (H, I) Detection and quantification of intracellular Fe^{2+} using FerroOrange staining (scale bar: 20μm; n = 3). (J, K) Western blot analysis of ferroptosis-related proteins and quantification using ImageJ (n = 3). (L, M) MitoSOX fluorescence staining was used to detect and quantify mitochondrial ROS accumulation (scale bar: 100μm; n = 3). (N, O) JC-1 staining for mitochondrial membrane potential, showing quantification of red/green fluorescent intensity (scale bar: 200μm; n = 3). (P) Representative TEM images showing mitochondrial ultrastructure in NPCs. Data are presented as the mean ± SD. ***p < 0.001; ns, not significant.

NSUN2 deposits m5C on Fth1 mRNA, thereby preserving its stability

To identify the downstream targets of NSUN2 in ferroptosis, we performed RNA bisulfite sequencing coupled with transcriptomic analysis on NPCs overexpressing wild-type NSUN2, and identified a panel of ferroptosis-related genes with altered RNA methylation levels. Bisulfite treatment deaminates unmethylated cytosines to uracil, while methylated cytosines remain unaltered. As illustrated in Figure 3A, NSUN2 overexpression led to a markedly increased m5C modified levels, among which *Fth1* displayed the most prominent hypermethylation. Moreover, mRNA transcriptomic profiling revealed that *Fth1* was the most significantly upregulated gene upon NSUN2 overexpression (Figure 3B, C). Western blot confirmed that FTH1 protein levels were remarkably replenished by wild-type NSUN2 but not enzymatic-dead NSUN2 in NPCs with erastin treatment (Figure 3D, E). These findings indicate *Fth1* is a potential target of NSUN2 in ferroptosis regulation. To investigate whether NSUN2 directly interacts with *Fth1* mRNA, we carried out RNA immunoprecipitation (RIP) followed by RT-

qPCR analysis. This revealed a substantial enrichment of *Fth1* transcripts in the NSUN2 RIP samples relative to the control immunoprecipitates (Figure 3F). As NSUN2 is a main mRNA methyltransferase catalyzing m5C formation, we tested whether NSUN2 promoted FTH1 translation through the m5C modification of *Fth1* mRNA. The results showed that, the overexpression of NSUN2 increased m5C methylation levels of *Fth1* mRNA (Figure 3G). In erastin-treated cells, m5C levels of *Fth1* mRNA significantly decreased in parallel with reductions in NSUN2 protein levels (Figure 3H). In addition, RNA stability assays demonstrated that the knockdown of NSUN2 resulted in decreased stability of *Fth1* mRNA, whereas overexpression of NSUN2 significantly increased it; however, the enzymatic-dead mutant NSUN2 failed to confer such protection (Figure 3I, J). Since NSUN2-mediated m5C modifications are predominantly located within the 3′ untranslated region (3′ UTR) of RNA, we performed an *in vitro* methylation analysis of the *Fth1* 3′ UTR to pinpoint the principal NSUN2-catalysed methylation sites. This analysis identified cytosine 785 (C785) as a major m5C site in NPCs, with a methylation level of 7%. Overexpression of NSUN2 in NPCs significantly increased the methylation rate at C785 compared with that in control cells (Figure 3K). Subsequently, to verify whether the m5C modification at C785 of *Fth1* mRNA mediates the NSUN2-induced enhancement of FTH1 translation, we introduced a point mutation at this methylation site in the *Luci-M-3'UTR* reporter construct. Overexpression of NSUN2 led to a marked increase in luciferase activity from the *Luci-M-3'UTR*, whereas the activity of the *Luci-M-C785T* mutant remained unaffected (Figure 3L). Immunohistochemical (IHC) analysis of human NP tissues revealed a progressive decline in FTH1 expression as IVDD progressed, accompanied by a positive correlation between FTH1 and NSUN2 levels in these specimens (Figure 3M-O). These findings collectively demonstrate that *Fth1* mRNA is subject to NSUN2-mediated methylation, with the critical m5C site residing at C785 within its 3′ UTR.

YBX1 recognizes m5C modification of Fth1 mRNA to enhance FTH1 expression

Previous studies have established that recognition of m5C-methylated mRNA sites by reader proteins is required for enhanced transcript stability[37, 38, 49]. To identify the stable reader responsible for *Fth1* mRNA stability, RNA pull-down assays were performed using *in vitro*-transcribed biotinylated probes or m5C-*Fth1* RNA probes, followed by mass spectrometry (MS) to identify probe-specific binding proteins. YBX1, a well-characterized m5C reader, was robustly enriched with the RNA-protein complexes, indicating a direct and selective binding affinity for m5C-methylated *Fth1* transcripts (Figure 4A). To verify whether NSUN2-mediated m5C methylation impacts the interaction between YBX1 and *Fth1* mRNA in ferroptosis, the binding ability of YBX1 to *Fth1* mRNA was examined in erastin-treated cells. The results indicated a decrease in the interaction between YBX1 and *Fth1* mRNA in erastin-treated cells following downregulation of NSUN2. Notably, the YBX1-*Fth1* mRNA interaction in erastin-treated cells was rescued by the replenishment of WT NSUN2 but not the enzymatic-dead NSUN2 mutant (Figure 4B). However, mutation of the m5C sites within *Fth1* abrogated YBX1 binding to the transcript (Figure 4C). Correspondingly, act-D chase experiments demonstrated that knockdown of YBX1 shortened the half-life of *Fth1* mRNA (Figure 4D). YBX1 recognizes and binds to m5C-methylated sites on mRNA through its cold shock domain (CSD), thereby promoting transcript stability[50]. To assess whether the CSD is essential for the maintenance of m5C-modified *Fth1* mRNA, we generated three YBX1 expression constructs encoding Flag-tagged, full-length YBX1, and a CSD domain-deletion mutant (ΔCSD), respectively. Our results showed that overexpression of the CSD-deleted YBX1 failed to elevate FTH1 protein levels (Figure 4E). Similarly, RIP assays confirmed that *Fth1* transcripts were enriched with full-length YBX1, but not with the YBX1 mutant lacking the CSD domain (Figure 4 F). Western blot analysis revealed that knockdown of YBX1 upregulated the expression of IVDD markers (MMP3 and MMP13) and ferroptosis markers (ACSL4 and PTGS2), whereas overexpression of YBX1 increased the levels of Collagen II, Aggrecan, GPX4 and FTH1 (Figure 4 G-I and Figure S5A-E). IHC analysis of human NP tissues revealed that YBX1 expression progressively declined as IVDD progressed, and that YBX1 levels were positively correlated with NSUN2 levels in human NP tissues (Figure 4J-L). Collectively, these results underscore a key role for YBX1 in sustaining *Fth1* mRNA stability.

Overexpression of NSUN2 significantly alleviates the progression of IVDD *in vivo*

Building on our findings that NSUN2 suppresses ferroptosis to counteract IVDD, we next evaluated its therapeutic potential *in vivo*. In a rat model of IVDD established by tail-needle puncture, NSUN2 was overexpressed via intradiscal delivery of adeno-associated virus (AAV) encoding NSUN2 (Figure 5A). X-ray analysis revealed that needle puncture induced a marked loss of disc height relative to controls, whereas overexpression of NSUN2 significantly rescued this degenerative reduction (Figure 5B, C).

Consistently, T2-weighted MRI further demonstrated that NSUN2 overexpression restored both the signal intensity and hydration status of the disc (Figure 5D, E). Histological analysis revealed that needle puncture induced marked disruption of the nucleus pulposus architecture, accompanied by loss of proteoglycans and disorganization of collagen architecture. These pathological changes were significantly ameliorated upon AAV-NSUN2 delivery (Figure 5F and Figure 5M). Consistently, IHC staining demonstrated that needle puncture markedly upregulated MMP13 expression while downregulating Collagen II and NSUN2 in the NPCs. While, overexpression of NSUN2 substantially reversed these effects (Figure 5G-L). Western blot analysis further confirmed these results (Figure S6A, B).

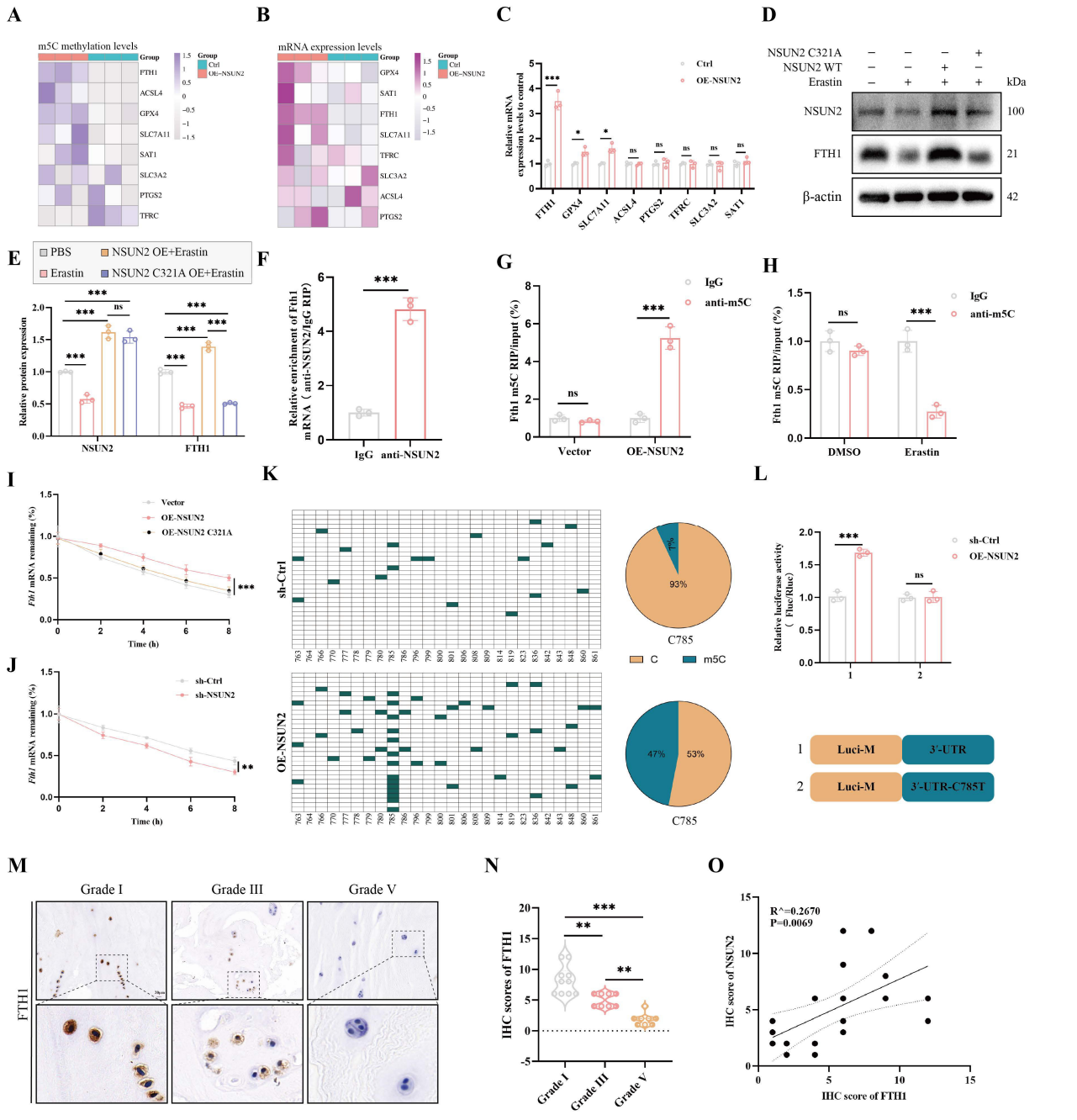

Figure 3. NSUN2-mediated *Fth1* mRNA m5C methylation enhances FTH1 protein expression. (A) m5C modification levels of ferroptosis-related genes in RNA bisulfite sequencing data (n = 3). (B) The mRNA levels of different ferroptosis-related genes in transcriptome sequencing results (n = 3). (C) Quantitative PCR was conducted to detect the mRNA expression of ferroptosis-related genes in NSUN2 overexpression NPCs (n = 3). (D, E) Western blot was used to evaluate the protein levels of NSUN2 and FTH1 after NSUN2 overexpression (n = 3). (F-H) RIP/qPCR was carried out to evaluate the binding of NSUN2 to *Fth1* mRNA (n = 3). (I, J) *Fth1* mRNA half-life was assessed by actinomycin D chase assay in NSUN2-knockdown or NSUN2-overexpressing NPCs (n = 3). (K) Methylated (green) and unmethylated (white) cytosine positions were mapped by RNA bisulfite sequencing in control or NSUN2-overexpressing cells (n = 3). (L) NPCs were transfected with the indicated luciferase reporter plasmids, followed by luciferase activity assay (n = 3). (M, N) Representative images of anti-FTH1 immunohistochemical staining and comparison of IHC scores among different Pfirrmann scores (n = 10 patients in Grade I, n = 8 patients in Grade III and n = 8 patients in Grade V). (O) The Spearman correlation scatter plot of IHC scores for NSUN2 and FTH1 (n = 26). Data are presented as the mean ± SD. *p < 0.05, **p < 0.01, ***p < 0.001.

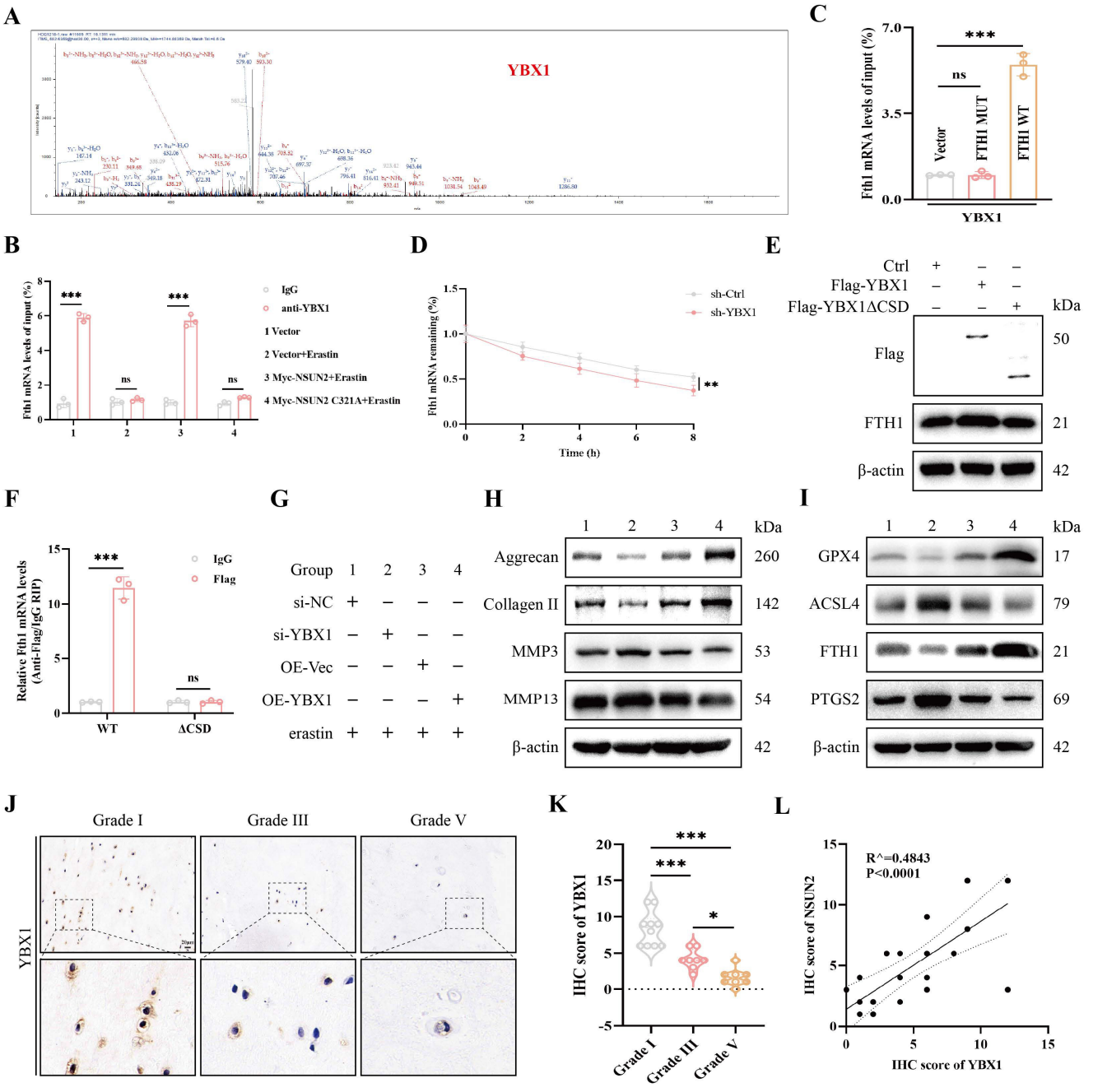

Figure 4. YBX1 recognizes m5C modification of *Fth1* and stabilizes *Fth1* mRNA. (A) Mass spectrometry identified YBX1 as a specific interactor of m5C modified *Fth1* RNA probes. (B) NPCs with or without the expression of Myc-NSUN2 or NSUN2 (C321A) were treated with erastin, and then the interactions between YBX1 and *Fth1* mRNA were detected by RIP assays. (C) *Fth1* mRNA half-life was assessed by actinomycin D chase assay in YBX1-knockdown NPCs (n = 3). (D) Real-time PCR of RIP assays in NPCs showed that YBX1 directly associated with wild-type (WT) *FTH1* mRNA, but not the mutant (MUT) transcript harboring mutations at the key methylation sites (n = 3). (E) Western blot analysis of FTH1 protein levels in NPCs expressing YBX1 (full-length or CSD-deleted) (n = 3). (F) RIP assays evaluate the binding between full-length or CSD-deleted YBX1 and *Fth1* mRNA (n = 3). (G-I) Representative western blots showing expression levels of IVDD-related and ferroptosis-related indicators after knockdown or overexpression of YBX1 in NPCs (n = 3). (J, K) Representative images of anti-YBX1 immunohistochemical staining and comparison of IHC scores among different Pfirrmann scores (n = 10 patients in Grade I, n = 8 patients in Grade III and n = 8 patients in Grade V). (L) The Spearman correlation scatter plot of IHC scores for NSUN2 and YBX1 (n = 26). Data are presented as the mean ± SD. *p < 0.05, **p < 0.01, ***p < 0.001.

We next profiled the levels of ferroptosis-related markers *in vivo*. Needle puncture resulted in a pronounced increase in MDA and Fe^{2+} accumulation, accompanied by a substantial depletion of GSH content (Figure S6E-G). Western blot analysis revealed that puncture significantly reduced the expression of GPX4 and FTH1, but elevated that of ACSL4 and PTGS2, findings that were further validated by IHC staining (Figure 5G-J and Figure S6C, D). Collectively, these results indicated that ferroptosis was prominently activated in the IVDD model. Importantly, all these changes were significantly reversed by NSUN2 overexpression. Overall, our *in vivo* findings demonstrate that AAV-NSUN2 delivery

effectively suppresses ferroptosis in NPCs and mitigates puncture-induced disc degeneration, positioning NSUN2 as a promising therapeutic target for IVDD.

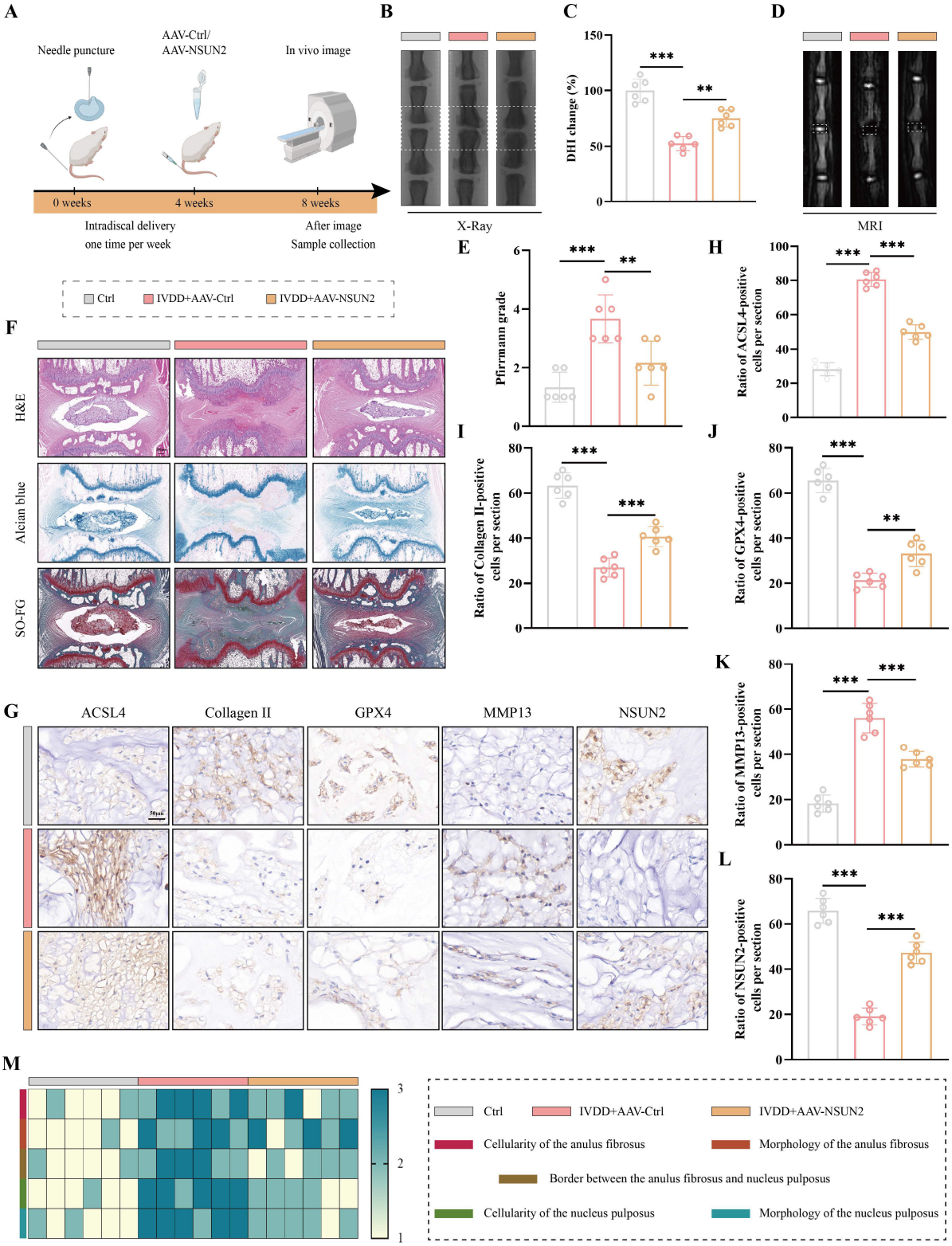

Figure 5. Overexpression of NSUN2 mitigates rat IVDD. (A) Schematic illustration of the experimental design. (B, C) X-ray images and quantification of disc height index (DHI) in rat treated with intradiscal injection of AAV-vec or AAV-NSUN2 (n = 6). (D, E) Representative MRI images of rat treated with intradiscal injection of AAV-vec or AAV-NSUN2 (n = 6). (F) Representative histological staining of H&E, SO-FG and Alcian blue staining in rat treated with intradiscal injection of AAV-vec or AAV-NSUN2 (scale bar: 200 μm; n = 6). (G-L) Immunohistochemical staining of ACSL4, Collagen II, GPX4, MMP13 and NSUN2 in rat discs, with quantitative analysis of immunohistochemical staining (scale bar: 50 μm; n = 6). (M) Plot of histological scores of each experimental group in heatmap format (n = 6). Data are presented as the mean ± SD. **p < 0.01, ***p < 0.001.

TRIM25 interacts with NSUN2

We next investigated the mechanism underlying the downregulation of NSUN2 during ferroptosis. Cycloheximide (CHX) chase assays revealed that the half-life of NSUN2 protein was markedly shortened in erastin-treated NPCs (Figure 6A, B). Furthermore, treatment with the proteasome inhibitor MG132 effectively prevented the erastin-induced decline in NSUN2 protein levels, whereas the autophagy inhibitor bafilomycin A1 (Baf A1) did not (Figure 6C). Furthermore, ubiquitination of NSUN2 was markedly increased in erastin-treated NPCs, reinforcing that NSUN2 is degraded via the ubiquitin-proteasome pathway during ferroptosis. To pinpoint the E3 ubiquitin ligase responsible for this degradation, we conducted IP coupled with MS (IP/MS), which identified TRIM25 as a strong interactor (Figure 6E, F). Western blot analysis further demonstrated that erastin upregulated TRIM25 protein levels in a dose-dependent manner (Figure 6G). Co-IP experiments confirmed this finding, showing that TRIM25 precipitated NSUN2 but not IgG in NPCs (Figure 6H). Reverse Co-IP further validated that NSUN2 effectively binds to and precipitates TRIM25 in NPCs (Figure 6I). To verify this interaction, we co-transfected HEK 293T cells with Flag-tagged TRIM25 and Myc-tagged NSUN2, and then performed Co-IP using antibodies against the respective tags. As expected, Flag-tagged TRIM25 showed a strong interaction with Myc-tagged NSUN2 in HEK 293T cells (Figure 6J, K). Moreover, compared with controls, both the protein levels of NSUN2 and its association with TRIM25 were markedly decreased in erastin-treated NPCs and in NP tissues from the rat model of IVDD (Figure 6L, M). To precisely map the interaction domains, we generated a series of truncated Flag-tagged TRIM25 and Myc-tagged NSUN2 fragments and evaluated their binding in HEK 293T cells (Figure 6N). A fragment comprising the amino acids 1-223 within the N terminus of TRIM25 was found to associate with NSUN2 (Figure 6O). Furthermore, Co-IP analysis revealed that the NSUN2 fragment spanning residues 209-614 specifically interacted with TRIM25 (Figure 6P). Collectively, these data confirm a physical interaction between TRIM25 and NSUN2.

TRIM25 mediates the ubiquitination and degradation of NSUN2 in NPCs ferroptosis

Next, we assessed the effect of TRIM25 silencing on NSUN2 expression levels in NPCs. Knockdown of TRIM25 increased NSUN2 protein levels, particularly in erastin-treated cells (Figure 7A, B). To determine whether the E3 ligase activity of TRIM25 is required for this process, we generated a mutant (TRIM25-Mut) carrying a point mutation (R45P) in the critical catalytic site of its RING domain, as previously reported[39]. Functional assays showed that overexpression of wild-type TRIM25 accelerated NSUN2 degradation, whereas the mutant did not (Figure 7C). CHX chase assays showed that knockdown of TRIM25 extended the half-life of NSUN2, whereas overexpression of TRIM25 accelerated its degradation (Figure 7D-G). These results further confirmed that TRIM25 degrades NSUN2 in a proteasome-dependent manner. We next carried out additional experiments to determine whether TRIM25 regulates NSUN2 ubiquitination and subsequent turnover. Compared with sh-NC, knockdown of TRIM25 substantially increased NSUN2 protein levels and concomitantly reduced its ubiquitination (Figure 7H, I). To validate the role of TRIM25 in mediating NSUN2 ubiquitination, we co-transfected HEK 293T cells with Myc-NSUN2, Flag-TRIM25 (wild-type or the R45P mutant) and HA-Ub. We found that exogenous overexpression of wild-type TRIM25, but not the R45P mutant, markedly enhanced NSUN2 ubiquitination (Figure 7J, K). To further substantiate the role of TRIM25 in NSUN2 degradation during ferroptosis, we examined TRIM25-mediated NSUN2 ubiquitination in erastin-treated cells. The results showed that erastin treatment markedly enhanced TRIM25-mediated ubiquitination of NSUN2 (Figure 7L, M). Moreover, in both the sham and IVDD groups, delivery of AAV-TRIM25 significantly reduced NSUN2 protein levels and increased its ubiquitination compared with AAV-Ctrl (Figure 7N, O). We further investigated the effect of TRIM25 on the linkage type of polyubiquitin chains conjugated to NSUN2. Western blot analysis revealed that TRIM25 specifically promoted Lys48-linked polyubiquitination of NSUN2, without substantially affecting Lys63-linked chains (Figure 7P). To confirm that Lys48-linked ubiquitination is critical for TRIM25-mediated NSUN2 degradation, we expressed a Lys48-resistant ubiquitin mutant (Lys48R) in TRIM25-knockdown HEK293T cells. Expression of Lys48R completely abolished the upregulation of NSUN2 protein levels induced by TRIM25 knockdown (Figure 7Q), highlighting the essential role of Lys48-linked ubiquitination in this regulatory axis. Collectively, these findings demonstrate that TRIM25 governs NSUN2 stability in NPCs by modulating its ubiquitination and subsequent proteasomal degradation.

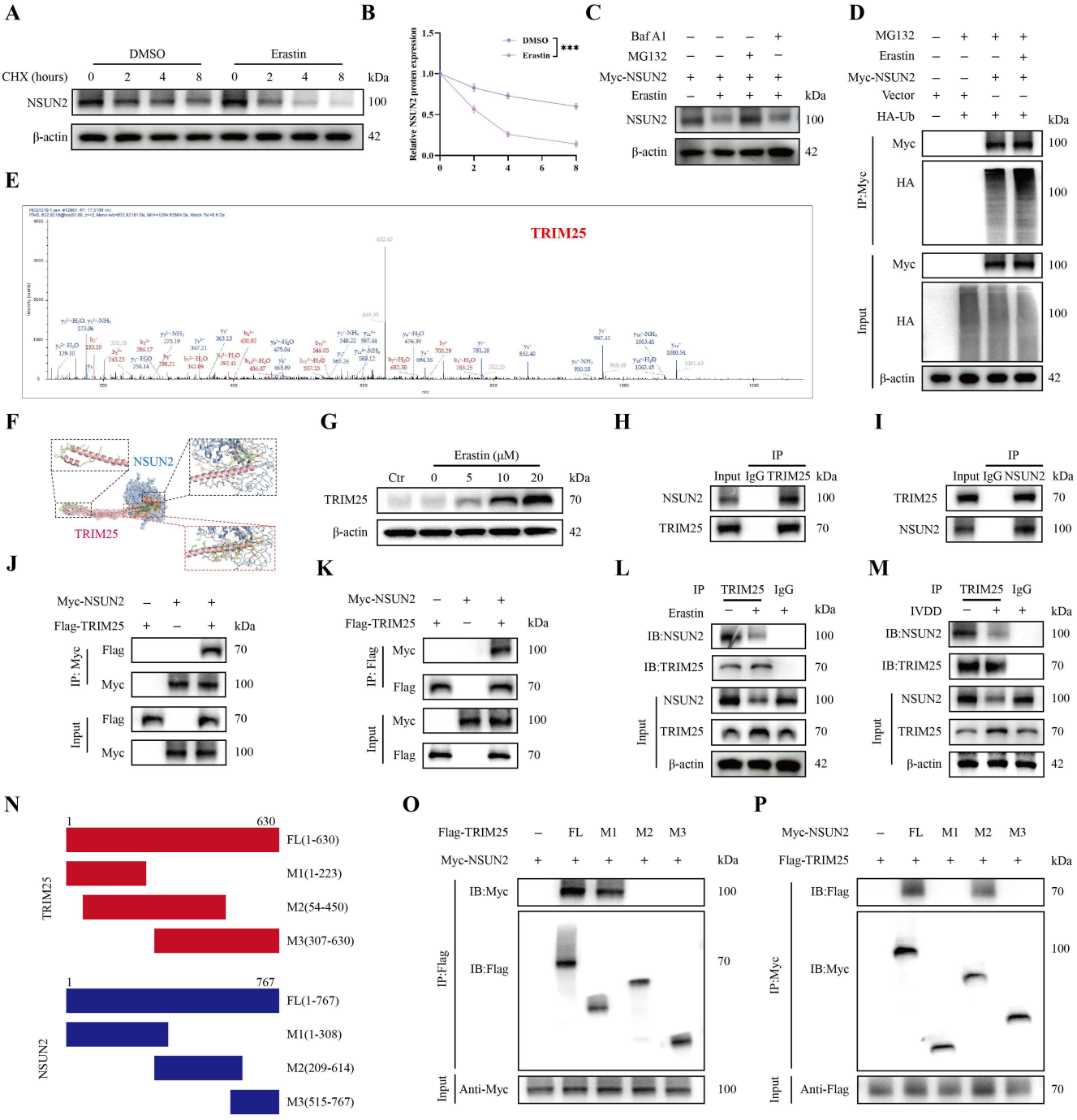

Figure 6. TRIM25 interacts with NSUN2 in NPCs. (A, B) NPCs with or without erastin treatment were incubated with CHX for indicated times, and then the protein levels of NSUN2 were detected by western blot (n = 3). (C) NSUN2 protein levels were assessed by western blot in NPCs treated by erastin together with MG132 or Baf A1 (n = 3). (D) Myc-NSUN2 and HA-Ub were co-immunoprecipitated from MG132-treated NPC lysates with anti-Myc, and blotted for the indicated proteins (n = 3). (E, F) IP/MS and molecular docking confirmed the interaction between TRIM25 and NSUN2. (G) Representative western blot showing the protein level of TRIM25 after erastin treatment (n = 3). (H, I) Co-IP and Reverse Co-IP indicated that TRIM25 interacts with NSUN2 in NPCs. (J, K) Exogenous Flag-tagged TRIM25 and Myc-tagged NSUN2 efficiently co-precipitated in HEK293T cells. (L) Co-IP of TRIM25 and NSUN2 in NPCs treated with or without erastin (n = 3). (M) Co-IP of TRIM25 and NSUN2 in NP tissues from rat with or without IVDD (n = 3). (N) Schematic representation of full-length (FL) and various deletion mutants of tagged TRIM25 or NSUN2. (O) The Co-IP revealed that the fragment containing M1 domain of TRIM25 was able to bind NSUN2. (P) Reverse Co-IP proved that TRIM25 interacted with M2 domain of NSUN2. Data are presented as the mean ± SD. ***p < 0.001.

Knockdown of TRIM25 attenuates ferroptosis induced by NSUN2 deficiency

To investigate whether TRIM25 regulates ferroptosis through NSUN2, we treated NPCs with sh-TRIM25 and sh-NSUN2 (Figure 8A). Knockdown efficiencies were confirmed by western blot and PCR (Figure 8B and Figure S7A-C). Dot blot assays revealed that knockdown of NSUN2 led to a decrease in m5C methylation levels regardless of TRIM25 knockdown. However, knockdown of TRIM25 markedly restored the reduction in m5C methylation caused by NSUN2

knockdown (Figure 8C). Similarly, knockdown of NSUN2 significantly inhibited cell viability, whereas knockdown of TRIM25 rescued this inhibitory effect (Figure S7D-F). Western blot analysis of IVDD-related markers yielded consistent results. Knockdown of NSUN2 alone reduced the expression of Aggrecan and Collagen II, while upregulating MMP3 and MMP13 (Figure S7J, K). Knockdown of TRIM25 alone produced the opposite effects (Figure S7J, K). Notably, concurrent knockdown of both TRIM25 and NSUN2 significantly alleviated the suppression of the anabolic components Aggrecan and Collagen II induced by NSUN2 knockdown (Figure S7J, K). Next, we assessed several key markers of ferroptosis. As expected, knockdown of NSUN2 alone increased the accumulation of MDA, lipid peroxidation, intracellular ROS and Fe^{2+}, accompanied by a decline in GSH. In contrast, knockdown of TRIM25 alone significantly reversed these ferroptotic phenotypes. However, concurrent depletion of both TRIM25 and NSUN2 markedly abolished the protective effect of TRIM25 knockdown against ferroptosis in NPCs (Figure 8D-I and Figure S7G, H). Western blot analysis further confirmed these findings (Figure 8J, K).

Mitochondrial function was then assessed. Knockdown of NSUN2 significantly increased mitochondrial superoxide levels, whereas simultaneous knockdown of TRIM25 markedly reduced these levels (Figure 8L, M). JC-1 staining revealed that TRIM25 knockdown rescued the decrease in mitochondrial membrane potential induced by NSUN2 knockdown (Figure 8N, O). Similar results were further confirmed by Mito Tracker staining, showing that TRIM25 knockdown ameliorated the mitochondrial dysfunction caused by NSUN2 knockdown (Figure S7I). TEM imaging further confirmed that NSUN2 knockdown caused severe mitochondrial ultrastructural abnormalities, including cristae disruption and outer membrane alterations, whereas TRIM25 knockdown largely reversed these defects (Figure 8P). Collectively, these results indicate that TRIM25 knockdown mitigates the mitochondrial integrity impairment induced by NSUN2 knockdown and alleviates ferroptosis-related damage, further supporting the notion that TRIM25 regulates ferroptosis in NPCs through modulation of NSUN2 protein levels.

Knockdown of TRIM25 significantly alleviates the progression of IVDD *in vivo*

We further evaluated the therapeutic potential of targeting TRIM25 *in vivo*. Following the establishment of the IVDD model, animals received direct intradiscal injections of either AAV-shCtrl or AAV-shTRIM25 (Figure 9A). Radiographic analysis revealed that the IVDD surgery caused a marked loss of disc height, which was significantly preserved by AAV-shTRIM25 delivery (Figure 9B, C). Consistently, T2-weighted MRI showed that AAV-shTRIM25 administration substantially restored signal intensity and hydration levels (Figure 9D, E). Histological assessments using H&E, Safranin O-Fast Green and Alcian blue staining demonstrated that the IVDD operation resulted in severe disruption of disc architecture and depletion of proteoglycans and collagen. In contrast, AAV-shTRIM25 delivery effectively restored structural integrity and promoted ECM deposition (Figure 9F-M). IHC analysis revealed that AAV-shTRIM25 treatment led to reduced expression of the degeneration-related marker MMP13, accompanied by increased levels of Collagen II (Figure 9G, I, K). These findings were further corroborated by western blot (Figure S8A, B). Collectively, these results support a protective role for TRIM25 knockdown in preserving disc architecture and promoting anabolic ECM metabolism.

To further evaluate the status of ferroptosis *in vivo*, we performed ELISA on NP tissues. Quantitative analysis revealed that IVDD surgery induced accumulation of MDA and Fe^{2+}, accompanied by a reduction in GSH content, while AAV-shTRIM25 treatment significantly reversed these changes (Figure S8E-G). IHC staining confirmed that AAV-shTRIM25 markedly decreased ACSL4 expression and restored GPX4 levels (Figure 9G, H, J). Consistently, we found that AAV-shTRIM25 significantly upregulated FTH1 levels (Figure S9A, B). Notably, AAV-shTRIM25 administration also restored NSUN2 expression in NPCs (Figure 9G, L). Western blot analysis further corroborated these observations, demonstrating upregulation of GPX4 and FTH1, alongside downregulation of ACSL4 and PTGS2 upon TRIM25 knockdown (Figure S8C, D).

Collectively, these findings demonstrate that knockdown of TRIM25 significantly upregulates NSUN2 protein expression by suppressing its ubiquitin-mediated degradation. This in turn stabilizes the m5C methylation modification of the downstream FTH1 transcript and ultimately elevates FTH1 protein abundance. This regulatory axis effectively enhances ferroptosis resistance in NPCs and attenuates the progression of IVDD both *in vitro* and *in vivo*, providing robust preclinical evidence for the therapeutic potential of targeting TRIM25 in IVDD.

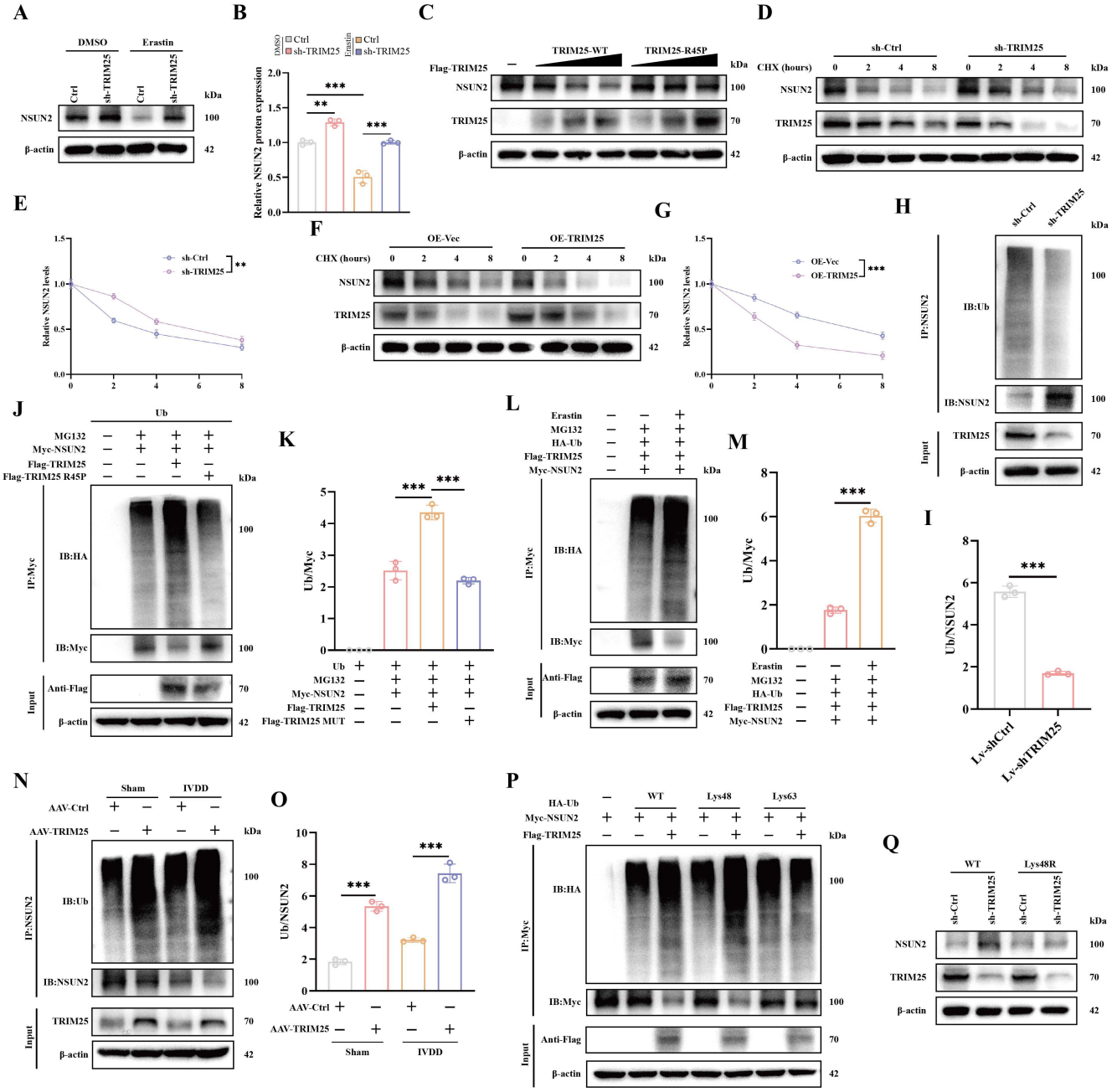

Figure 7. TRIM25 catalyzes NSUN2 ubiquitination and promotes its degradation in ferroptosis. (A, B) NPCs with or without TRIM25 knockdown were treated with erastin, and then NSUN2 protein levels were detected by western blot (n = 3). (C) Transfection of Flag-tagged TRIM25 (WT or R45P mutant) into HEK 293T cells, followed by immunoblotting with anti-NSUN2 and anti-Flag antibodies (n = 3). (D-G) NSUN2 stability was evaluated in NPCs subjected to either TRIM25 knockdown or overexpression, respectively (n = 3). (H, I) Western blot was performed to determine the changes in NSUN2 protein abundance and ubiquitination upon TRIM25 knockdown (n = 3). (J, K) Myc-NSUN2, HA-Ub, and Flag-TRIM25 or its R45P mutant were expressed in NPCs. Co-IP was performed using anti-Myc antibody in lysates from cells treated with MG132 followed by immunoblotting for Myc-NSUN2 and HA-Ub. (L, M) NPCs expressing Myc-NSUN2, HA-Ub, and Flag-TRIM25 were treated with or without erastin in the presence of MG132. Co-IP was performed using anti-Myc antibody in cell lysates followed by immunoblotting for Myc-NSUN2 and HA-Ub (n = 3). (N, O) NP tissue lysates from rats injected with AAV-Ctrl or AAV-TRIM25 were immunoprecipitated with anti-NSUN2 (n = 3). (P) HEK 293T cells were co-transfected with Myc-NSUN2, Flag-TRIM25 and HA-Ub, Lys48 alone, or Lys63 alone plasmids, and then NSUN2 ubiquitination was analyzed (n = 3). (Q) HEK 293T cells transfected with ubiquitin WT or ubiquitin K48R were cultured in the presence of shCtrl or shTRIM25 for 72 h. Cell lysates were assessed by immunoblotting with anti-NSUN2 and anti-TRIM25 (n = 3). Data are presented as the mean ± SD. **p < 0.01, ***p < 0.001.

Discussion

In this study, we identify a previously unrecognized TRIM25-NSUN2-FTH1 signalling axis that drives ferroptosis in NPCs and accelerates IVDD. Our findings establish that NSUN2, a key methyltransferase for mRNA m5C modification, is markedly downregulated in degenerated human NP tissues, and that its loss sensitizes NPCs to ferroptosis through diminished m5C methylation of *Fth1* mRNA, leading to reduced FTH1 protein expression. Mechanistically, we demonstrate that the E3 ubiquitin ligase TRIM25 directly interacts with NSUN2 and

promotes its Lys48-linked polyubiquitination and proteasomal degradation, thereby suppressing NSUN2 levels during ferroptosis. The m5C reader YBX1 recognizes the methylated *Fth1* transcript and preserves its stability; this protective axis is disrupted upon NSUN2 degradation. Importantly, genetic silencing of TRIM25 *in vivo* restores NSUN2 expression, enhances m5C methylation of *Fth1* mRNA, elevates FTH1 protein abundance and attenuates IVDD progression in a rat model. Collectively, these findings define a novel molecular pathway coupling ubiquitin-mediated degradation of an m5C methyltransferase to ferroptosis susceptibility in NPCs, and position TRIM25 as a potential therapeutic target for IVDD.

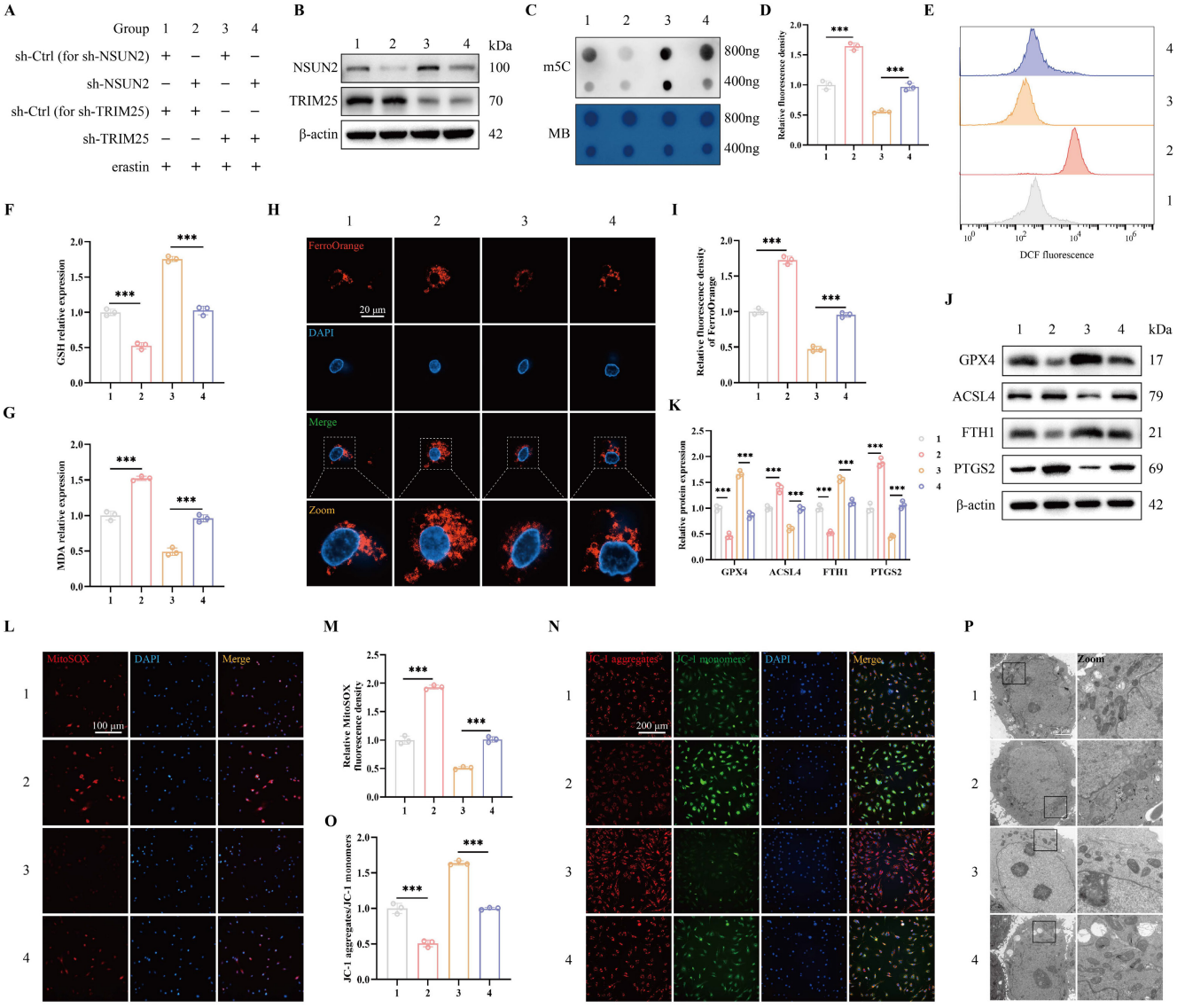

Figure 8. Knockdown of TRIM25 attenuates ferroptosis induced by NSUN2 deficiency in NPCs. (A) Detailed information of experimental assignment. (B) The transfection efficiency was confirmed by western blot analysis (n = 3). (C) Dot blot assay was used to assess m5C levels in NPCs. (D-G) ROS, GSH and MDA concentrations were measured (n = 3). (H, I) Detection and quantification of intracellular Fe^{2+} using FerroOrange staining (scale bar: 20μm; n = 3). (J, K) Western blot analysis of ferroptosis-related proteins and quantification using Image J (n = 3). (L, M) MitoSOX fluorescence staining was used to detect and quantify mitochondrial ROS accumulation (scale bar: 100μm; n = 3). (N, O) JC-1 staining for mitochondrial membrane potential, showing quantification of red/green fluorescent intensity (scale bar: 200μm; n = 3). (P) Representative TEM images showing mitochondrial ultrastructure in NPCs. Data are presented as the mean ± SD. ***p < 0.001.

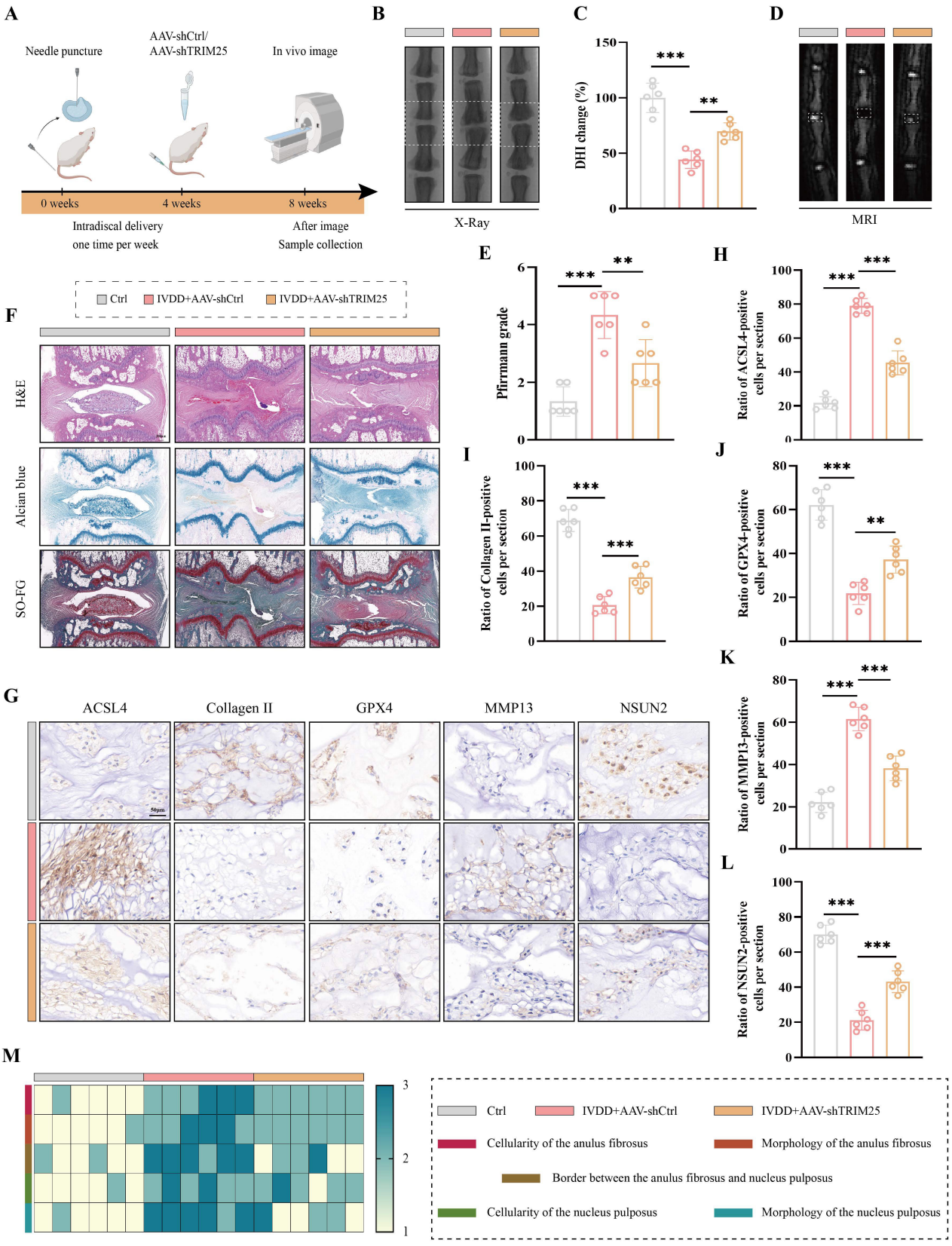

Figure 9. Knockdown of TRIM25 ameliorates rat IVDD. (A) Schematic illustration of the experimental design. (B, C) X-ray images and quantification of DHI in rat treated with intradiscal injection of AAV-shCtrl or AAV-shTRIM25 (n = 6). (D, E) Representative MRI images of rat treated with intradiscal injection of AAV-shCtrl or AAV-shTRIM25 (n = 6). (F) Representative histological staining of H&E, SO-FG and Alcian blue staining in rat treated with intradiscal injection of AAV-shCtrl or AAV-shTRIM25 (scale bar: 200 μm; n = 6). (G-L) Immunohistochemical staining of ACSL4, Collagen II, GPX4, MMP13 and NSUN2 in rat discs, with quantitative analysis of immunohistochemical staining (scale bar: 50 μm; n = 6). (M) Plot of histological scores of each experimental group in heatmap format (n = 6). Data are presented as the mean ± SD. **p < 0.01, ***p < 0.001.

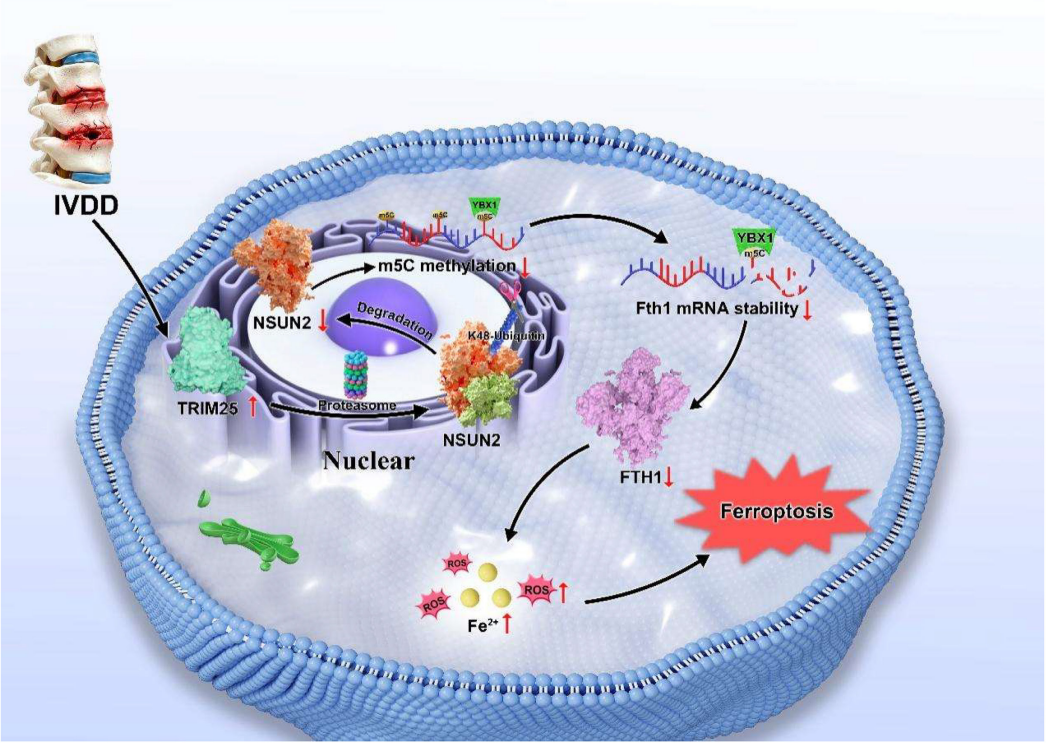

Figure 10. Schematic illustration of the TRIM25-NSUN2-FTH1 axis regulating ferroptosis in NPCs. TRIM25-mediated ubiquitination downregulates NSUN2, leading to reduced m5C methylation of *Fth1* mRNA and decreased FTH1 protein levels, which in turn sensitizes NPCs to ferroptosis both *in vitro* and *in vivo*.

Ferroptosis has emerged as a critical driver of NPCS loss in IVDD, yet the upstream regulatory networks that initiate this cell death program within the unique disc microenvironment remain incompletely understood[13]. Recent studies have identified several ferroptosis-modulating pathways in IVDD, including the UCHL3-HMGB1-NCOA4 axis that activates ferritinophagy[23], the USP11-Sirt3 cascade that counteracts oxidative stress-induced ferroptosis[2], and the FBXO2-LCN2 axis that suppresses ferroptosis through ubiquitination of a pro-ferroptotic factor[12]. However, the involvement of RNA modifications, particularly m5C methylation, in ferroptosis regulation during IVDD has not been previously explored. Our study fills this gap by demonstrating that the m5C methyltransferase NSUN2 acts as a critical suppressor of ferroptosis in NPCs, and that its downregulation is a key event linking oxidative stress to ferroptosis. This finding expands the conceptual framework of ferroptosis regulation beyond protein-centric mechanisms to encompass epitranscriptomic control, highlighting the importance of RNA modifications in determining cellular susceptibility to ferroptosis[27, 38, 49].

The discovery that NSUN2-mediated m5C methylation of *Fth1* mRNA sustains FTH1 expression provides a mechanistic link between RNA modification and iron homeostasis, a central determinant of ferroptosis sensitivity. FTH1, the heavy chain of ferritin, sequesters intracellular labile iron and thereby limits Fenton reaction-mediated lipid peroxidation[51]. Our data demonstrate that NSUN2 deposits m5C at cytosine 785 within the 3′ untranslated region of *Fth1* mRNA, and that this modification is recognized by the m5C reader YBX1, which stabilizes the transcript and promotes FTH1 translation. This NSUN2-YBX1-FTH1 axis thus represents a previously unknown regulatory layer governing iron storage capacity in NPCs. The functional significance of this axis is underscored by our observation that loss of NSUN2 or YBX1 recapitulates the ferroptotic phenotype, whereas overexpression of wild-type NSUN2, but not its catalytically dead mutant, rescues FTH1 expression and protects against ferroptosis. These findings align with emerging evidence that m5C modification of mRNAs encoding antioxidant and iron-metabolism genes can modulate cellular stress responses[31, 33, 49], and extend this paradigm to the context of disc degeneration.

Our identification of TRIM25 as the E3 ubiquitin ligase responsible for NSUN2 degradation during ferroptosis reveals a critical node connecting ubiquitin-proteasome signalling to epitranscriptomic regulation. TRIM25, a well-characterized E3 ligase involved in innate immunity and tumorigenesis[43, 45], has not previously been implicated in the regulation of RNA methylation machinery. In a study conducted by

Wu et al., they found that TRIM25 mediates the ubiquitination of XRCC1, thereby upregulating PARP1, which in turn activates macrophage M1 polarization and necroptosis, accelerating aortic inflammation and the progression of atherosclerotic plaques[46]. Shang and colleagues indicated that TRIM25 could co-condense with the stress granule core protein G3BP1 in a manner of liquid-liquid phase separation, thereby enhancing the ubiquitination activity of TRIM25 toward multiple antiviral proteins primarily localized in stress granules, which activates downstream signaling pathways and ultimately inhibits RNA virus infection[44]. Similarly, Liu et al. reported that TRIM25 promotes the survival and growth of hepatocellular carcinoma by targeting Keap1 for ubiquitination and degradation[45]. In our study, we show that TRIM25 directly binds NSUN2 and promotes Lys48-linked polyubiquitination, targeting NSUN2 for proteasomal degradation. Notably, erastin-induced ferroptosis upregulates TRIM25 expression and enhances its ubiquitination and degradation of NSUN2, resulting in a significant reduction in NSUN2 protein levels and the steady-state TRIM25-NSUN2 complex, suggesting that oxidative stress actively engages this degradative pathway to suppress the protective m5C methylation program. This is reminiscent of the stress-induced downregulation of other epitranscriptomic regulators, such as METTL3 and ALKBH5[27, 52-54], under pathological conditions, but our study provides the first evidence that an E3 ligase directly controls the stability of an m5C methyltransferase in response to ferroptotic signals. The functional relevance of this regulation is demonstrated by our rescue experiments: knockdown of TRIM25 restores NSUN2 expression, elevates m5C methylation of *Fth1* mRNA, and effectively counteracts ferroptosis, whereas reconstitution of NSUN2 is required for this protective effect. Collectively, these data position TRIM25 as a gatekeeper that, when upregulated, dismantles the NSUN2-FTH1 antioxidant shield and primes NPCs for ferroptosis.

The translational implications of our findings are substantial. Current therapeutic strategies for IVDD are largely palliative, and disease-modifying interventions that target the underlying molecular mechanisms are urgently needed[15, 17, 55-57]. Our *in vivo* data demonstrate that AAV-mediated overexpression of NSUN2 or knockdown of TRIM25 effectively attenuates IVDD progression in a rat needle-puncture model, preserving disc height, hydration and extracellular matrix integrity while suppressing ferroptosis markers. These results provide preclinical proof-of-concept that targeting the TRIM25-NSUN2 axis is therapeutically viable. Notably, the dual benefit of TRIM25 knockdown, restoring NSUN2 expression while directly mitigating the ubiquitin-proteasome degradation of this protective methyltransferase, offers a more targeted approach than global antioxidant strategies, which may have off-target effects. However, several challenges must be addressed before clinical translation. First, the specificity of TRIM25 inhibition requires careful evaluation, as TRIM25 has diverse substrates beyond NSUN2[45, 46]. Tissue-specific delivery strategies, such as the polydopamine-based nanoplatform could enhance therapeutic efficacy while minimizing systemic toxicity[15]. Second, the long-term consequences of sustained NSUN2 upregulation or TRIM25 knockdown on disc homeostasis and adjacent tissues need to be rigorously assessed in large-animal models.

Several limitations of our study warrant stated. First, although our experiments were conducted in human primary NPCs and rat IVDD models, the translational relevance of the TRIM25-NSUN2-FTH1 axis should be validated in larger animal models, such as rabbits or pigs, whose disc anatomy more closely resembles that of humans. Second, while we focused on *Fth1* mRNA as a key downstream target of NSUN2, our transcriptomic and methylomic analyses identified additional ferroptosis-related genes with altered m5C modification upon NSUN2 overexpression. It is possible that NSUN2 exerts its protective effects through a network of m5C-modified transcripts, and comprehensive mapping of these targets may reveal additional regulatory nodes that could be exploited therapeutically. Third, the upstream signals that drive TRIM25 upregulation during IVDD, whether inflammatory cytokines, mechanical overload, or oxidative stress, remain to be elucidated. Understanding these initiating events could uncover earlier intervention points for preventing NSUN2 loss and ferroptosis activation. Fourth, although we established that YBX1 is a reader of m5C-modified *Fth1* mRNA, we cannot exclude the involvement of other m5C readers, such as ALYREF or SBP2, in modulating *Fth1* mRNA transcript stability or translation in NPCs. Further studies are needed to dissect the full complement of readers and their context-dependent contributions.

Despite these limitations, our study provides several conceptual advances. First, it establishes epitranscriptomic regulation, specifically NSUN2-mediated m5C methylation, as a previously unrecognized determinant of ferroptosis susceptibility in NPCs, expanding the known repertoire of ferroptosis-modulating mechanisms beyond protein phosphorylation, ubiquitination and lipid metabolism. Second, it identifies TRIM25 as a novel E3

ligase that bridges the ubiquitin-proteasome system to the epitranscriptome, revealing a previously unknown layer of crosstalk between post-translational and post-transcriptional regulation. Third, it positions the TRIM25-NSUN2-FTH1 axis as a promising therapeutic target for IVDD, offering a mechanistic rationale for developing disease-modifying interventions that enhance NPCs resistance to ferroptosis.

In conclusion, we have uncovered a novel molecular pathway in which TRIM25-mediated ubiquitination and degradation of NSUN2 suppresses m5C methylation of *Fth1* mRNA, reduces FTH1 expression and promotes ferroptosis in NPCs, thereby accelerating IVDD progression (Figure 10). Our findings provide new insights into the pathogenesis of disc degeneration and identify TRIM25 and NSUN2 as potential therapeutic targets for this prevalent and disabling condition. Future studies aimed at developing selective inhibitors of TRIM25 or stabilizing NSUN2 expression may pave the way for effective disease-modifying therapies for IVDD and associated low back pain.

Abbreviations

IVDD: Intervertebral disc degeneration; NPCs: nucleus pulposus cells; m5C: 5-methylcytosine; IP/MS: immunoprecipitation-mass spectrometry; ECM: extracellular matrix; ROS: reactive oxygen species; PTMs: post-translational modifications; DUBs: deubiquitinating enzymes; NSUN2: NOL1/NOP2/Sun RNA methyltransferase 2; TRIM25: tripartite motif containing 25; MDA: malondialdehyde; GSH: glutathione; Co-IP: co-immunoprecipitation; H&E: Hematoxylin and Eosin; SO-FG: safranin O&Fast Green; IHC: immunohistochemistry.

Supplementary Material

Supplementary figures and tables.
https://www.ijbs.com/v23p0640s1.pdf

Acknowledgements

This work was supported by Beijing Natural Science Foundation (L254007), National Natural Science Foundation of China (82572800), Beijing Hospital Management Center 'Yangfan' Program for Clinical Technology Innovation Projects (ZLRK202517), National Key Research & Development Program of China (grant ID: 2025YFC2511600), National Natural Science Foundation of China (12502375) and Cultivation Project of Capital Medical University (PYZ25051).

Data available

Raw data are available from the corresponding authors on reasonable request.

Author contributions

Peng Cui: conceptualisation, formal analysis, investigation, methodology, visualisation, writing-original draft, writing-review and editing. Tao Hu: investigation, methodology, writing-original draft. Qingyang Huang: investigation, software, writing-original draft. Yijian Zhang: investigation, software, writing-original draft. Xuan Zhao: data curation, formal analysis. Haojie Zhang: software, resources. Fumin Pan: software, resources. Chao Kong: software, resources. Ruizhang Yao: software, resources. Yuluo Rong: supervision. Jiaxiang Bai: supervision, resources. Haixia Huang: supervision, resources. Yongjin Li: conceptualisation, funding acquisition, supervision, writing-review and editing. Peng Wang: conceptualisation, funding acquisition, supervision, writing-review and editing. Xiaolong Chen: conceptualisation, funding acquisition, supervision, writing-review and editing. Shibao Lu: conceptualisation, funding acquisition, supervision, writing-review and editing.

Competing Interests

The authors have declared that no competing interest exists.

References

1. Vollset SE, Ababneh HS, Abate YH, et al. Burden of disease scenarios for 204 countries and territories, 2022–2050: a forecasting analysis for the Global Burden of Disease Study 2021. The Lancet. 2024; 403(10440): 2204-2256.
2. Zhu J, Sun R, Sun K, et al. The deubiquitinase USP11 ameliorates intervertebral disc degeneration by regulating oxidative stress-induced ferroptosis via deubiquitinating and stabilizing Sirt3. Redox Biology. 2023; 62(102707.
3. Zhang W, Li G, Zhou X, et al. Disassembly of the TRIM56-ATR complex promotes cytoDNA/cGAS/STING axis–dependent intervertebral disc inflammatory degeneration. Journal of Clinical Investigation. 2024; 134(6): e165140.
4. Sun K, Shi Y, Yan C, et al. Glycolysis-Derived Lactate Induces ACSL4 Expression and Lactylation to Activate Ferroptosis during Intervertebral Disc Degeneration. Advanced Science. 2025; 12(21): e2416149.
5. Lu X, Li D, Lin Z, et al. HIF-1 α -induced expression of the m6A reader YTHDF1 inhibits the ferroptosis of nucleus pulposus cells by promoting SLC7A11 translation. Aging Cell. 2024; 23(9): e14210.
6. Li H, Tang Y, Liu Z, et al. Lumbar instability remodels cartilage endplate to induce intervertebral disc degeneration by recruiting osteoclasts via Hippo-CCL3 signaling. Bone Research. 2024; 12(1): 34.
7. Xia Q, Zhao Y, Dong H, et al. Progress in the study of molecular mechanisms of intervertebral disc degeneration. Biomedicine & Pharmacotherapy. 2024; 174(116593.
8. B W Koes, M W van Tulder and Thomas S Diagnosis and treatment of low back pain. BMJ. 2006; 332(1430-1434.
9. Kaneda G, Zila L, Wechsler JT, et al. What a pain in the back: etiology, diagnosis and future treatment directions for discogenic low back pain. Bone Research. 2025; 13(1): 89.
10. Diwan AD and Melrose J Intervertebral disc degeneration and how it leads to low back pain. Jor Spine. 2022; 6(1): e1171.
11. Huang Y, Xiao B, Liang H, et al. A CREB5-NR4A1 checkpoint protects against disc degeneration by controlling ferroptosis. Osteoarthritis and Cartilage. 2026; 34(7): 1046-1062.
12. Wu T, Wang Y, Shen B, et al. FBXO2 Alleviates Intervertebral Disc Degeneration via Dual Mechanisms: Activating PINK1-Parkin Mitophagy and Ubiquitinating LCN2 to Suppress Ferroptosis. Advanced Science. 2025; 12(36): e06150.

13. Chen J, Yang X, Li Q, et al. Inhibiting DNA methyltransferase DNMT3B confers protection against ferroptosis in nucleus pulposus and ameliorates intervertebral disc degeneration via upregulating SLC40A1. Free Radical Biology and Medicine. 2024; 220(139-153.
14. Xiang Z, Zhang P, Jia C, et al. Piezo1 channel exaggerates ferroptosis of nucleus pulposus cells by mediating mechanical stress-induced iron influx. Bone Research. 2024; 12(1): 20.
15. Yang X, Chen Y, Guo J, et al. Polydopamine Nanoparticles Targeting Ferroptosis Mitigate Intervertebral Disc Degeneration Via Reactive Oxygen Species Depletion, Iron Ions Chelation, and GPX4 Ubiquitination Suppression. Advanced Science. 2023; 10(13): e2207216.
16. Zhou L-P, Kang L, Zhang Z-G, et al. RBX1 mitigates ferroptosis by inhibiting NCOA4-mediated ferritinophagy and contributes to the attenuation of intervertebral disc degeneration. Journal of Translational Medicine. 2025; 23(1): 514.
17. Gao T, Xu G, Ma T, et al. ROS-Responsive Injectable Hydrogel Loaded with SLC7A11-modRNA Inhibits Ferroptosis and Mitigates Intervertebral Disc Degeneration in Rats. Advanced Healthcare Materials. 2024; 13(27): e2401103.
18. Zhang Y, Han S, Kong M, et al. Single-cell RNA-seq analysis identifies unique chondrocyte subsets and reveals involvement of ferroptosis in human intervertebral disc degeneration. Osteoarthritis and Cartilage. 2021; 29(9): 1324-1334.
19. Wu T, Teng Y, Song D, et al. A strategy targeting ferroptosis for mitochondrial reprogramming and intervertebral disc degeneration therapy. Theranostics. 2025; 15(17): 9159-9178.
20. Ruan B, Dong J, Wei F, et al. DNMT aberration-incurred GPX4 suppression prompts osteoblast ferroptosis and osteoporosis. Bone Research. 2024; 12(1): 68.
21. Wang L, Yin G, Li W, et al. Steap4 Promotes Senile Osteoporosis via Fe2+-ROS/C/EBP β Feedback-Driven Ferroptosis and Adipogenesis in Senescent BMSCs. Advanced Science. 2025; 13(5): e09926.
22. Liang H, Zhu D, Du Z, et al. Dysregulated methylation–ubiquitination crosstalk accelerates intervertebral disc degeneration via MED12 destabilization and cGAS/STING activation. Journal of Clinical Investigation. 2026; e197274.
23. Hu T, Cui P, Zhao X, et al. UCHL3 drives ferroptosis in nucleus pulposus cells by deubiquitinating HMGB1 to activate NCOA4-mediated ferritinophagy. Autophagy. 2026; 1-21.
24. Zhu D, Liang H, Tong B, et al. DDX1 methylation mediated MATR3 splicing regulates intervertebral disc degeneration by initiating chromatin reprogramming. Nature Communications. 2025; 16(1): 6153.
25. Kong K, Li B, Chang Y, et al. Delivery of FGF18 using mRNA-LNP protects the cartilage against degeneration via alleviating chondrocyte senescence. Journal of Nanobiotechnology. 2025; 23(1): 34.
26. Roundtree IA, Evans ME, Pan T, et al. Dynamic RNA Modifications in Gene Expression Regulation. Cell. 2017; 169(7): 1187-1200.
27. Wu O, Jin Y, Zhang Z, et al. KMT2A regulates the autophagy-GATA4 axis through METTL3-mediated m6A modification of ATG4a to promote NPCs senescence and IVDD progression. Bone Research. 2024; 12(1): 67.
28. Chen Z, Song J, Xie L, et al. N6-methyladenosine hypomethylation of circGPATCH2L regulates DNA damage and apoptosis through TRIM28 in intervertebral disc degeneration. Cell Death & Differentiation. 2023; 30(8): 1957-1972.
29. Chen D, Gu X, Nurzat Y, et al. Writers, readers, and erasers RNA modifications and drug resistance in cancer. Molecular Cancer. 2024; 23(1): 178.
30. Meng H, Miao H, Zhang Y, et al. YBX1 promotes homologous recombination and resistance to platinum-induced stress in ovarian cancer by recognizing m5C modification. Cancer Letters. 2024; 597(217064.
31. Zhang H, Zhai X, Liu Y, et al. NOP2-mediated m5C Modification of c-Myc in an EIF3A-Dependent Manner to Reprogram Glucose Metabolism and Promote Hepatocellular Carcinoma Progression. Research. 2023; 6(0184.
32. Chen B, Deng Y, Hong Y, et al. Metabolic Recoding of NSUN2-Mediated m5C Modification Promotes the Progression of Colorectal Cancer via the NSUN2/YBX1/m5C-ENO1 Positive Feedback Loop. Advanced Science. 2024; 11(28): e2309840.
33. Moon J, Lee H, Jang Y, et al. NSUN-Mediated m5C RNA Modification in Stem Cell Regulation. Cells. 2025; 14(20): 1609.
34. Chen T, Xu Z-G, Luo J, et al. NSUN2 is a glucose sensor suppressing cGAS/STING to maintain tumorigenesis and immunotherapy resistance. Cell Metabolism. 2023; 35(10): 1782-1798.e8.
35. Hu Y, Chen C, Tong X, et al. NSUN2 modified by SUMO-2/3 promotes gastric cancer progression and regulates mRNA m5C methylation. Cell Death & Disease. 2021; 12(9): 842.
36. Ye W, Zhao Y, Zhou Y, et al. NSUN2-mediated cytosine-5 methylation of FSP1 protects acute myeloid leukemia cells from ferroptosis. Molecular Cancer. 2025; 24(1): 201.
37. Suo X, Zhang M, Zhu Q, et al. NSUN2-mediated GATM m5C methylation regulates creatine metabolism to drive mitochondrial fission and promote renal fibrosis. Cell Reports. 2026; 45(4): 117253.
38. Zhang X, Zhang Y, Li R, et al. STUB1-mediated ubiquitination and degradation of NSUN2 promotes hepatocyte ferroptosis by decreasing m5C methylation of Gpx4 mRNA. Cell Reports. 2024; 43(11): 114885.
39. Cheng Z, Gao H, Wu W, et al. Elevated TRIM25 Impairs Poly (ADP-ribose) Metabolism via PARG Degradation and Mediates Compression-Induced Intervertebral Disc Degeneration. Advanced Science. 2026; 13(25): e19248.
40. Wu Z, Jiang Z, Hong C, et al. Acetylation Regulates ACSL4 Degradation Through Chaperone-Mediated Autophagy to Alleviate Intervertebral Disc Degeneration. Advanced Science. 2025; 13(8): e16015.
41. Wu Z, Yang S, Jiang Z, et al. UCHL1 alleviates nucleus pulposus cell senescence by promoting chaperone-mediated autophagy antagonizing autophagy-dependent ferroptosis through deubiquitination of HSPA8. Autophagy. 2025; 21(12): 2842-2866.
42. Zhu D, Liang H, Du Z, et al. Altered Metabolism and Inflammation Driven by Post-translational Modifications in Intervertebral Disc Degeneration. Research. 2024; 7(0350.
43. Martín-Vicente M, Medrano LM, Resino S, et al. TRIM25 in the Regulation of the Antiviral Innate Immunity. Frontiers in Immunology. 2017; 8(1187.
44. Shang Z, Zhang S, Wang J, et al. TRIM25 predominately associates with anti-viral stress granules. Nature Communications. 2024; 15(1): 4127.
45. Liu Y, Tao S, Liao L, et al. TRIM25 promotes the cell survival and growth of hepatocellular carcinoma through targeting Keap1-Nrf2 pathway. Nature Communications. 2020; 11(1): 348.
46. Wu H, Gao W, Ma Y, et al. TRIM25-mediated XRCC1 ubiquitination accelerates atherosclerosis by inducing macrophage M1 polarization and programmed death. Inflammation Research. 2024; 73(9): 1445-1458.
47. Jia S, Liu H, Yang T, et al. Single-cell sequencing reveals cellular heterogeneity of nucleus pulposus in intervertebral disc degeneration. Scientific Reports. 2024; 14(1): 27245.
48. Zhang W, Qin X, Li G, et al. Self-powered triboelectric-responsive microneedles with controllable release of optogenetically engineered extracellular vesicles for intervertebral disc degeneration repair. Nature Communications. 2024; 15(1): 5736.
49. Chen S-J, Zhang J, Zhou T, et al. Epigenetically upregulated NSUN2 confers ferroptosis resistance in endometrial cancer via m5C modification of SLC7A11 mRNA. Redox Biology. 2024; 69(102975.
50. Chen X, Li A, Sun B-F, et al. 5-methylcytosine promotes pathogenesis of bladder cancer through stabilizing mRNAs. Nature Cell Biology. 2019; 21(8): 978-990.
51. Zhang Z, Feng Y, Mu Z, et al. Huaier counteracts sorafenib resistance in hepatocellular carcinoma by activating NCOA4-mediated ferritinophagy to induce ferroptosis via modulation of iron and lipid metabolism. Biochimica et Biophysica Acta (BBA) - Molecular Basis of Disease. 2026; 1872(7): 168313.
52. Wu O, Jin Y, Weng S, et al. METTL3 regulates α-KG-dependent mitophagy and apoptosis in nucleus pulposus cells through the MALAT1/miR-23c/IDH1 axis. Cell Reports. 2026; 45(1): 116793.
53. Zhuang T, Chen M-H, Wu R-X, et al. ALKBH5-mediated m6A modification of IL-11 drives macrophage-to-myofibroblast transition and pathological cardiac fibrosis in mice. Nature Communications. 2024; 15(1): 1995.
54. Guo F, Fan J, Liu J-M, et al. Astrocytic ALKBH5 in stress response contributes to depressive-like behaviors in mice. Nature Communications. 2024; 15(1): 4347.
55. Wang X, Guo Z, Chen L, et al. Synergistic Modulating of Mitochondrial Transfer and Immune Microenvironment to Attenuate Discogenic Pain. Advanced Science. 2025; 12(23): e2500128.
56. Xie Z, Jiang B, Wang G, et al. Targeting AMPK signaling in nucleus pulposus cells ameliorates spaceflight microgravity-induced intervertebral disc degeneration. Cell Death & Differentiation. 2026.
57. Zhou H, Wu C, Jin Y, et al. Role of oxidative stress in mitochondrial dysfunction and their implications in intervertebral disc degeneration: Mechanisms and therapeutic strategies. Journal of Orthopaedic Translation. 2024; 49: 181-206.